INTERNATIONAL ATOMIC ENERGY AGENCY
UNITED NATIONS EDUCATIONAL, SCIENTIFIC AND CULTURAL ORGANIZATION

INTERNATIONAL CENTRE FOR THEORETICAL PHYSICS
34100 TRIESTE (ITALY) - P.O.B. 586 - MIRAMARE - STRADA COSTIERA 11 - TELEPHONE: 2240-1
CABLE: CENTRATOM - TELEX 460392 - I

INTERNATIONAL CENTRE FOR THEORETICAL PHYSICS
13 MAY 1987
LIBRARY

SMR/208 - 9

SPRING COLLEGE IN MATERIALS SCIENCE

ON

"METALLIC MATERIALS"

(11 May - 19 June 1987)

BACKGROUND MATERIAL FOR:
"HIGH TEMPERATURE MATERIALS (INCLUDING Ni-BASE SUPERALLOYS AND ORDERED INTERMETALLIC ALLOYS)

C.T. LIU
Chemical Division
Oakridge National Laboratory
Oakridge, Tennessee 37831
U.S.A.

These are preliminary lecture notes, intended only for distribution to participants.

Reprint Series
9 November 1984, Volume 226, pp. 636–642

SCIENCE

Ductile Ordered Intermetallic Alloys

C. T. Liu and J. O. Stiegler

Copyright © 1984 by the American Association for the Advancement of Science

Ductile Ordered Intermetallic Alloys

C. T. Liu and J. O. Stiegler

Summary. Many ordered intermetallic alloys have attractive high-temperature properties; however, low ductility and brittle fracture limit their use for structural applications. The embrittlement in these alloys is mainly caused by an insufficient number of slip systems (bulk brittleness) and poor grain-boundary cohesion. Recent studies have shown that the ductility and fabricability of ordered intermetallics can be substantially improved by alloying processes and control of microstructural features through rapid solidification and thermomechanical treatments. These results demonstrate that the brittleness problem associated with ordered intermetallics can be overcome by using physical metallurgical principles. Application of these principles will be illustrated by results on Ni_3Al and Ni_3V-Co_3V-Fe_3V. The potential for developing these alloys as a new class of high-temperature structural materials is discussed.

Ordered intermetallic alloys constitute a unique class of metallic materials which form long-range ordered crystal structures below their melting points (T_m) or critical ordering temperatures (T_c). The various atomic species in these alloys tend to occupy specific sublattice sites and form superlattice structures. The structures and properties of ordered intermetallics were studied extensively in the 1950's and 1960's, and as a result of these efforts many attractive properties were identified and characterized (*1–4*). In ordered lattices, dislocations travel in pairs or groups, and their motion is thus subject to certain constraints, particularly at elevated temperatures (*5*). In general, the strength of ordered intermetallics does not degrade rapidly with increasing temperature. In many cases, these alloys exhibit yield stresses that increase with test temperature (*5–8*) rather than decrease, as is common for conventional or disordered alloys. Long-range order produces stronger binding and closer packing between atoms. The restricted atom mobility generally leads to slower diffusion processes and better creep resistance in ordered lattices. Ordered intermetallics such as aluminides and silicides are usually resistant to oxidation and corrosion because of their ability to form compact, adherent oxide surface films that protect the base metal from excessive attack (*9*).

The interest in ordered intermetallic alloys subsided in the latter part of the 1960's because of severe embrittlement problems (*1–4, 10–12*). Many intermetallics are so brittle that they simply cannot be fabricated into useful structural components. Even when fabricated, their low fracture toughness severely limits their use in structural applications. The design of ordered intermetallic alloys has been studied at a number of laboratories, and such work (*13–21*) has shown that the ductility and fabricability of several intermetallic systems can be substantially improved through application of physical metallurgical principles. The success of these efforts has renewed the interest in ordered intermetallics, and is expected to encourage their development as a new class of structural materials for high-temperature applications.

This article summarizes current efforts in the design of ductile ordered intermetallic alloys. These materials are often designated as both ordered alloys and intermetallic compounds. The term "ordered alloys" commonly refers to alloys that form long-range ordered crystal structures at relatively low temperatures (say, $T_c < 700°C$) and are disordered at higher temperatures. The term "intermetallic compounds," on the other hand, generally designates strongly ordered alloys with specific alloy formulas and compositions (that is, line compounds). This review focuses on the class of strongly ordered alloys that are ordered over a range of composition and have appreciable solubility of additional elements, allowing us to use alloying principles to design ductile materials.

Brittleness of Ordered Intermetallics

Ordered intermetallic alloys generally exhibit low ductility and brittle fracture, which severely restrict their use as structural materials. The brittleness in a particular alloy can usually be attributed to either of two major causes, namely, an insufficient number of slip systems and grain-boundary weakness. Many ordered alloys that crystallize in low crystal symmetries simply do not offer enough slip systems to permit extensive plastic deformation. Examples of alloys exhibiting limited crystalline deformation include Co_3V (*10*), Ni_3V (*10*), Fe_3Al (*22*), NiAl (*23*), Ti_3Al (*11*), and TiAl (*24*).

C. T. Liu is a group leader and J. O. Stiegler is director of the Metals and Ceramics Division, Oak Ridge National Laboratory, Oak Ridge, Tennessee 37830.

In some cases adequate deformation modes exist, yet the materials are brittle because of easy crack propagation along grain boundaries. The nickel aluminide Ni_3Al is a classic example of such behavior. Single crystals of Ni_3Al are highly ductile but polycrystals are extremely brittle (*16, 23, 25*). In this case, the grain boundaries are intrinsically weak (*26*). Polycrystalline Ni_3Al prepared from high-purity metals exhibits brittle intergranular fracture, even though impurity segregation is insignificant. Many ordered intermetallics, like conventional alloys (*27*), can be embrittled because of strong segregation of harmful impurities to grain boundaries (*28, 29*). Recent studies of nickel aluminides with Auger electron spectroscopy evidenced that alloy stoichiometry strongly influences the segregation behavior of both trace and alloying elements, thereby affecting alloy ductility and fracture behavior (*26*).

Other factors that contribute to the low ductility of alloys with long-range order include restricted cross slip, high Peierls stress, difficulty in twinning, and impurity locking of dislocations. It is generally observed (*1*) that ordered alloys exhibit planar slip because of the restriction in cross slip of superlattice dislocations in an ordered lattice. In contrast, alloys in a disordered state (produced by rapid quenching above T_c) exhibit wavy slip due to extensive cross slip of screw dislocations. Planar slip causes higher stress concentrations at the end of slip bands and induces cracking during the early stages of plastic deformation. Formation of long-range order generally lowers crystal symmetry and increases the atomic packing density, both of which could lead to high frictional stresses opposing the motion of dislocations on slip planes. Deformation by twinning is thought to be difficult in ordered lattices, since twinning induces local disordering (*30*).

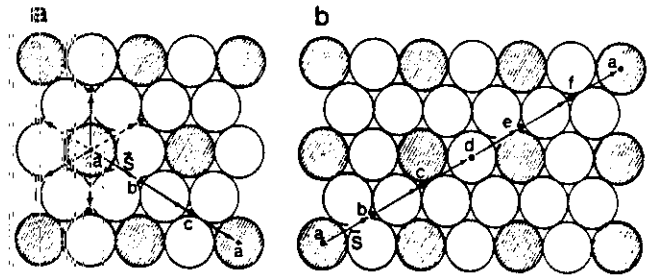

Fig. 1. Atomic structure of close-packed ordered planes: (a) triangular (T)-type ordered layer and (b) rectangular (R)-type ordered layer. (56).

Improvement of Ductility by Metallurgical Methods

Significant improvements in ductility and fabricability of ordered intermetallics have been achieved recently through alloying processes, innovative processing techniques, and thermomechanical treatments. Rapid solidification through melt-spinning, arc hammer, and rotating disk techniques has proved effective in improving the ductility of several aluminides, including Ni_3Al-B (*20, 31*), Ni-Al-X (*18*), FeAl (*21*), and Fe_3Al-TiB_2 (*32*). Recently, Inoue *et al.* (*18*) demonstrated that nickel aluminides with Ni-Al-X compositions (X = Fe, Mn, Cr, Si, and Co) can be made ductile and strong by a melt-spinning technique, while conventionally prepared alloys are extremely brittle. The beneficial effects of rapid solidification are attributed to several factors, including refinement of grain size, improvement in alloy homogeneity, elimination of grain-boundary segregation, and reduction in the degree of order. The disadvantages of rapid solidification are that products must be thin in at least one dimension and that they lose all or part of their favorable behavior during hot consolidation or subsequent heat treatment at elevated temperatures.

Several investigators (*17, 33, 34*) have attempted to improve the ductility of ordered intermetallics by thermomechanical treatments. Stoloff and Dillamore (*33*) reported a ductility of 20 percent for partially recrystallized FeCo–2 percent V specimens and only 5 percent for the fully recrystallized ones. Schulson and Baker (*17*) controlled the grain size by thermomechanical treatments and observed that NiAl exhibits a critical grain size below which polycrystalline aggregates are ductile in tension. This aluminide showed a tensile ductility of 40 percent at 400°C for a grain size less than a critical value of 20 μm. Recently, Stefanni and Liu (*35*) found that the tensile ductility of FeAl with 0.5 to 2 percent TiB_2 prepared by melting and casting can be increased moderately by control of recrystallization processes.

Both macroalloying and microalloying approaches have proved extremely effective in improving the ductility and fabricability of several ordered intermetallics. Macroalloying involves adding major concentrations (several percent or more) of alloying elements to control ordered crystal structures and bulk properties. Through control of alloy composition and electron concentration (*e/a*, the average number of electrons per atom outside the inert-gas shell), the ordered cubic structure of an $L1_2$ type has been stabilized for $(Ni,Co,Fe)_3V$, $(Ni,Co,Fe)_3V$, and $(Ni,Fe)_3V$ alloys, which have excellent ductility and fabricability (*18, 14*). In contrast, microalloying is the addition of minor concentrations (usually in the parts-per-million range) of elements to control grain-boundary composition and structure. Recent microalloying studies (*15, 16, 19*) have shown that the ductility of polycrystalline Ni_3Al can be dramatically improved by adding a few hundred parts per million of boron, which tends to segregate to grain boundaries and enhances their cohesion. The special promise of the alloying approach is that it does not rely on costly processing techniques such as rapid solidification, which have the disadvantages mentioned earlier. The alloying principles used in the design of ductile ordered intermetallics based on Co_3V and Ni_3Al are discussed in detail in the following sections.

Macroalloying and Control of Crystal Structures in Close-Packed A_3B Alloys

Bulk materials of many ordered intermetallics are brittle because of low-symmetry crystal structures that have limited numbers of slip systems. The ductility of these alloys can be substantially improved by control of ordered crystal structures—that is, changing the crystal structure from low symmetry (such as ordered hexagonal structure) to high symmetry (such as ordered cubic structure) through macroalloying. This section focuses on the use of alloying principles to control ordered crystal structures in close-packed alloys with A_3B compositions.

Many alloys of the general composition A_3B exist in ordered crystal structures (*36–41*) based on close-packed ordered layers, as shown in Fig. 1. These structures are built from the regular stacking of these layers. There are two basic types of close-packed ordered layers (*36*), designated as triangular (T) type and rectangular (R) type, as illustrated in Fig. 1, a and b, respectively. Stacking of the T layers gives ordered structures of cubic or hexagonal symmetry, depending on the stacking sequence. Some transition structures are complicated, with unit cells extending over 15 layers (*40*). Ordered structures formed by stacking

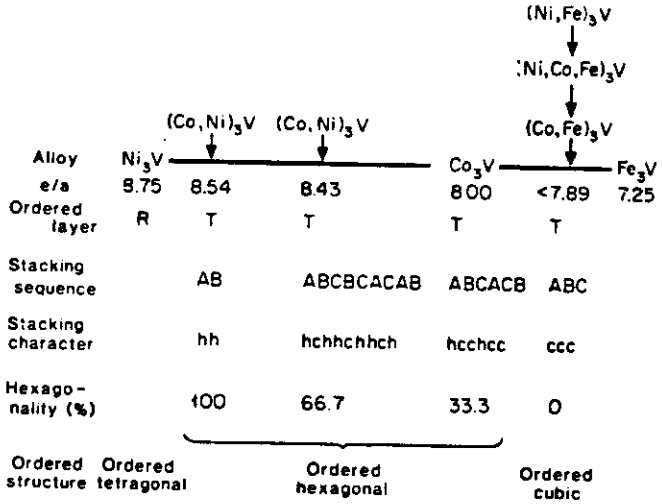

Fig. 2. Effect of electron concentration (e/a) on the stability of ordered crystal structures in Ni_3V-Co_3V-Fe_3V alloys.

of R layers generally have tetragonal symmetry.

Systematic studies of close-packed ordered A_3B structures have revealed that the stacking character in many pseudobinary alloys can be correlated with two fundamental alloying variables (*42*): atomic size and electron concentration. VanVucht and Buschow (*40, 41*) noted a general correlation between the stacking character of each layer and the radius ratio of A and B atoms, R_A/R_B. A layer is characterized as hexagonal if the layers adjacent to it have the same stacking position. For example, with a stacking sequence *ABA*, the B layer is designated as hexagonal. On the other hand, the B layer is a cubic layer in a stacking sequence *ABC*, where its adjacent layers A and C have different stacking positions. As the ratio R_A/R_B decreases in A_3B ordered alloys, the stacking character changes from purely cubic, through different ordered mixtures of cubic and hexagonal layers, to purely hexagonal. The change in the stacking character can be rationalized from consideration of space packing density. In the classic study of VanVucht and Buschow (*40*), the atomic radius of rare-earth elements (R) was correlated with the stacking character of trialuminides (Al_3R). With the decrease in atomic size, the hexagonal stacking decreases step by step from 100 percent (purely hexagonal ordered structure) to 0 percent (purely cubic ordered structure, $L1_2$ type).

Beck and Dwight (*36, 39*), on the other hand, correlated the stacking character of the T layer with the e/a ratio in alloys. With an increase in e/a, the ordered structure changes from predominantly cubic to predominantly hexagonal stacking. Further increase in e/a leads to a change in the basic layer structure from T to R type. Sinha (*43*) suggested that the electron effect may originate from the interaction of the electron concentration–dependent Fermi surface with the corresponding Brillouin zone.

The electron concentration correlation provides useful guidance in the control of ordered crystal structures of Co_3V macroalloyed with iron and cobalt. This is because Ni, Co, and Fe have similar atomic sizes and electronegativities but differ in e/a: 10, 9, and 8, respectively. The binary alloy Co_3V forms a six-layer hexagonal ordered structure (*38*) with the stacking sequence ABCACB. This structure can be best characterized as a transition structure, in which one-third of the T layers have a hexagonal (h) character and two-thirds a cubic (c) one. The stacking character of the six-layered Co_3V is therefore hcchcc, and its hexagonality is 33.3 percent.

Sinha (*37*) and Liu and Inouye (*13, 14*) found that the ordered crystal structure in Ni_3V-Co_3V-Fe_3V alloys can be correlated with e/a. The electron concentration in Co_3V can be increased by partial replacement of Co with Ni: $(Ni,Co)_3V$. With increase of e/a, the hexagonality of the ordered structure increases systematically from 33.3 to finally 100 percent (Fig. 2). Further increase in e/a above 8.54 produces a change in the basic layer structure from T type to R type (Fig. 1), and stacking of the R layers gives a tetragonal ordered structure similar to Ni_3V ($D0_{22}$). On the other hand, e/a in Co_3V can be reduced by partial substitution of Fe for Co: $(Co,Fe)_3V$. With an e/a below 7.89 the $L1_2$ ordered cubic structure having the stacking sequence ABC (ccc) is stabilized in $(Co,Fe)_3V$ alloys. All these observations agree well with the predictions from the electron concentration correlation.

Control of e/a provides considerable

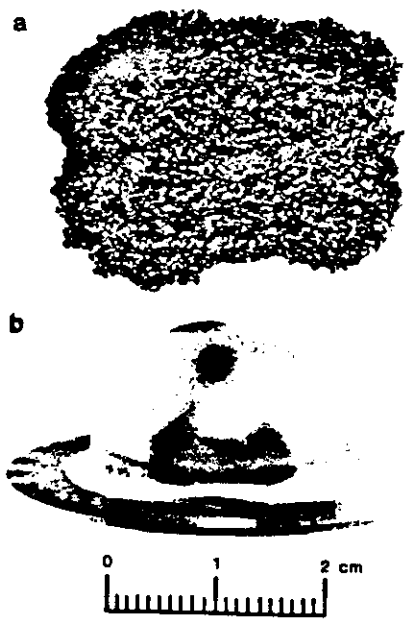

Fig. 3 (left). Comparison of the fabricability of unalloyed and boron-doped Ni_3Al alloys. (a) Fragmented appearance of an unalloyed Ni_3Al ingot hot-rolled at 1200°C, showing extensive grain-boundary cracking; and (b) a full cup of Ni_3Al with a boron content of 500 ppm by weight, deep-drawn at room temperature.

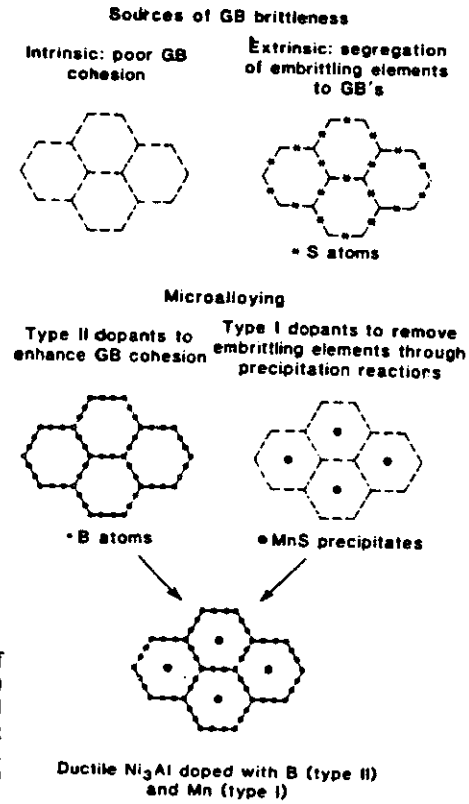

Fig. 4 (right). Sources of grain-boundary (GB) brittleness and design of ductile Ni_3Al by microalloying with type I and type II dopants

scope for alloy design. For instance, the cobalt content in $(Co,Fe)_3V$ can be reduced by replacing cobalt with an equal amount of an equiatomic mixture of nickel and iron. This scheme alters the alloy composition but not *e/a*. As indicated in Fig. 2, the ordered cubic structure remains stable in $(Ni,Co,Fe)_3V$ alloys as long as the electron concentration falls roughly in the same range as $(Co,Fe)_3V$. All cobalt atoms can be eventually replaced by nickel and iron atoms, resulting in ordered cubic alloys of the composition $(Ni,Fe)_3V$. With this scheme, the $L1_2$ structure is stabilized in $(Ni,Fe)_3V$ alloys without cobalt, an expensive strategic element. However, other properties such as the critical ordering temperature, T_c, are influenced by the alloy composition at a constant electron concentration.

The importance of the ordered cubic structure is shown by the room-temperature ductility of several ordered hexagonal and cubic alloys. Ordered cubic alloys of the compositions of $(Fe,Co)_3V$, $(Fe,Co,Ni)_3V$, and $(Fe,Ni)_3V$ are all ductile, with a tensile elongation of 40 percent or higher. However, the hexagonally ordered alloys Co_3V and $(Ni,Co)_3V$ are brittle with less than 1 percent elongation at room temperature. The deformation behavior of ordered cubic alloys is presumably similar to that of fcc materials having twelve {111} slip systems. The brittleness of ordered hexagonal alloys is mainly related to the limited number of slip systems available in ordered hexagonal crystal structures. The hexagonal alloys have ductilities too low to permit easy fabrication, while the cubic alloys have excellent fabricability at both room and elevated temperatures. The ability to control ordered crystal structure and ductility by alloying represents a major advance in alloy design.

Microalloying and Grain-Boundary Fracture in Nickel Aluminides

As mentioned earlier, low-symmetry crystal structures are not the only reason for embrittlement in ordered intermetallic alloys. Many intermetallics exhibit a brittleness that originates at grain boundaries. A classic example is Ni_3Al with an ordered cubic structure ($L1_2$). Single crystals of Ni_3Al are highly ductile, whereas polycrystals are extremely brittle at room and elevated temperatures because of the weakness of grain boundaries. This is illustrated in Fig. 3a, which shows a Ni_3Al ingot that cracked badly during hot rolling at 1200°C because of extensive cracking along grain boundaries.

Grain-boundary brittleness in Ni_3Al arises from two factors, as indicated in Fig. 4. The first, an intrinsic factor, is that the grain boundary is inherently weak relative to the grain interiors because of poor grain-boundary cohesion. That is, the high-purity aluminide exhibits brittle intergranular fracture without appreciable segregation of impurities at grain boundaries. The other, an extrinsic factor, is that segregation of certain impurities embrittles grain boundaries, as commonly observed in conventional alloys (*44*). Sulfur has been identified as a trace element that strongly segregates to grain boundaries in Ni_3Al and causes embrittlement (*45*).

Microalloying processes were used to overcome the grain-boundary brittleness problems. As illustrated in Fig. 4, two types of microalloying elements (dopants) were added to Ni_3Al. Type I dopants are reactive elements that bind harmful impurities such as sulfur in innocuous form through precipitation reactions. Type II dopants are elements that can act as electron donors (*46*, *47*), thereby increasing the cohesive strength of the boundary. Various dopants were added to Ni_3Al, including B, C, Ti, Ce, Ca, Mg, Mn, and Si. Of these dopants, boron is the most effective in improving the ductility and fabricability of Ni_3Al. Aoki and Izumi (*15*) first discovered the beneficial effect of boron in Ni_3Al and observed a tensile ductility of about 35 percent at room temperature. With control of the boron concentration, alloy stoichiometry, and thermomechanical treatment, Liu and Koch (*16*) obtained tensile elongations exceeding 50 percent for boron-doped Ni_3Al containing 24 atom percent Al. In practice, both type I and type II dopants are required to surmount the intrinsic and extrinsic grain-boundary problems. In this respect, additions of hafnium and manganese have been found to further improve the fabricability of boron-doped Ni_3Al.

Microalloyed Ni_3Al (24 atom percent Al) can best be fabricated at ambient temperature rather than at high temperatures. Sheets, rods, wires, and foils have been recently successfully cold-fabricated from small laboratory heats. Figure 3b shows a full cup of Ni_3Al with a boron content of 500 ppm by weight, deep-drawn at room temperature. The excellent formability stems from both the high ductility and rapid work hardening of the microalloyed aluminides.

The solubility limit for boron in Ni_3Al is greater than 2000 ppm by weight, and the beneficial effect arises from its presence in solution (*26*). Boron segregates strongly to grain boundaries, as evidenced by Auger spectra from freshly fractured grain-boundary surfaces. The boron signals very nearly disappear after sputtering the surface for 2 minutes, which removes only a few atom layers, indicating that boron is concentrated in a very narrow region adjacent to the grain

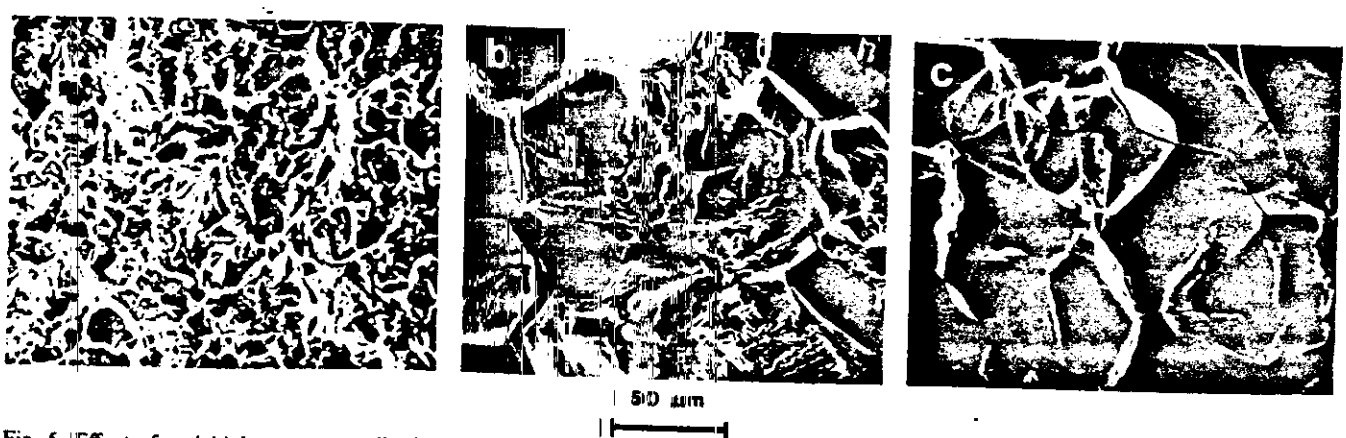

Fig. 5. Effect of stoichiometry on tensile ductility and fracture mode of boron-doped Ni_3Al tested at room temperature: (a) 24 percent Al, ductility = 49.4 percent, transgranular fracture; (b) 24.5 percent Al, ductility = 37.0 percent, mixed fracture mode; (c) 25.0 percent Al, ductility = 6.0 percent, intergranular fracture.

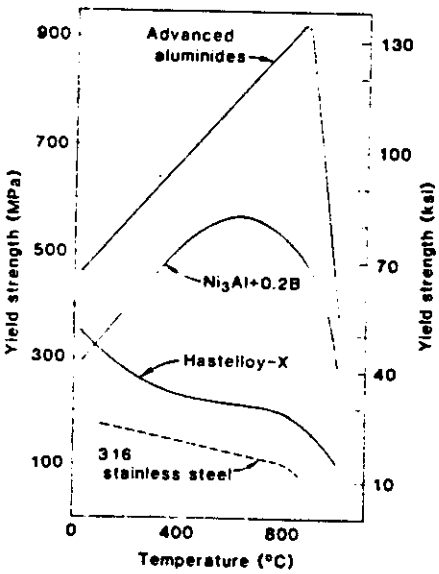

Fig. 6. Yield stress as a function of test temperatures for Ni_3Al-base aluminide alloys, Hastelloy X, and type 316 stainless steel.

boundary. The boron concentration is on the order of several percent, which greatly exceeds its bulk solubility limit. Transmission electron microscopy failed to reveal any precipitate particles, either at the boundaries or within the grains in boron-doped Ni_3Al.

Alloy stoichiometry has a strong effect on the ductility and fracture behavior of boron-doped Ni_3Al (*19*, *26*). Boron dopant is most effective in alloys containing 24 atom percent Al, and becomes less effective in Ni_3Al at higher concentrations. The beneficial effect, however, becomes less prominent in Ni_3Al at higher aluminum concentrations, as illustrated in Fig. 5. As the aluminum content of boron-doped Ni_3Al is increased from 24 to 25 atom percent, the fracture mode changes from transgranular (dimple-type), through a mixed mode, to intergranular. Correspondingly, there is a sharp decrease in the tensile ductility from above 50 to 6 percent. The studies of freshly fractured surfaces by Auger electron spectroscopy indicate that the aluminum content has no observable effects on C, O, and S segregation. Instead, boron segregation at grain boundaries decreases with increasing aluminum concentration. These observations suggest that the boron may become less effective in improving the ductility of Ni_3Al when there is less than a critical amount of boron present at the grain boundaries. Stoichiometry effects on the ductility of boron-doped Ni_3Al have also been observed in foil materials prepared by rapid solidification (*48*).

Considerable effort has been devoted to understanding the mechanism by which boron strengthens the grain boundaries. Quantum mechanical cluster calculations (*46*, *47*) have suggested that, in nickel, boron atoms act as electron donors and thereby strengthen the atomic bonding. At the same time, sulfur acts as an electron acceptor and weakens the bonding. In a recent study of boron-doped Ni_3Al, White and co-workers (*26*, *49*) observed unusual segregation behavior, with boron showing a strong tendency to segregate to the grain boundaries but not to free surfaces. This is in contrast to the usual observations that sulfur and other embrittling solutes tend to segregate more strongly to free surfaces than to grain boundaries. According to a classical thermodynamic theory of solute segregation effects on grain-boundary cohesion developed by Rice (*50*), the segregation behavior exhibited by boron should enhance grain-boundary cohesion and suppress intergranular fracture, in agreement with the observed effects of boron for Ni_3Al.

High-Temperature Properties of Ductile Ordered Intermetallic Alloys

The ductile ordered intermetallic alloys based on Ni_3Al and $(Fe,Co,Ni)_3V$ have attractive properties for structural uses at elevated temperatures. Figure 6 shows the unusual mechanical properties of Ni_3Al-base aluminides. The yield stress of boron-doped Ni_3Al increases rather than decreases with test temperature. Because of this increase, the aluminide becomes stronger than such commercial solid-solution alloys as Hastelloy X and type 316 stainless steel, whose strengths decrease with temperature. The yield strength of Ni_3Al begins to decrease above 600°C, and this decrease is not a result of thermal disordering; the material remains ordered up to its melting point (1390°C).

Similar increases in yield stress with temperature have been observed in $(Fe,Ni,Co)_3V$ (*14*), as well as in other $L1_2$ ordered alloys (*1*, *8*). Of the various models that have been suggested to explain such behavior, the cross slip model proposed by Kear and Wilsdorf (*51*, *52*) and Takeuchi and Kuramoto (*5*) is the most successful for describing the yield behavior of Ni_3Al (*53*). The model assumes a lower energy for an antiphase boundary (APB; the area defects where two ordered domains impinge on each other) on {100} planes than on {111} planes. A recent study of the APB morphology of as-quenched and annealed Ni_3Al foils produced by rapid solidification shows alignment of the APB's along

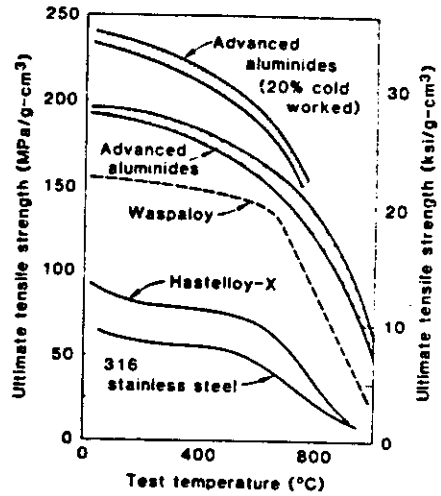

Fig. 7. Comparison of density-compensated ultimate tensile strength (as a function of temperature) of advanced aluminide alloys (boron-doped Ni_3Al plus 0.5 to 1.0 atom percent hafnium) with commercial alloys.

{100} planes, and provides the first direct experimental evidence (*54*) for the cross slip model. The drop in yield stress above 600°C results from a gradual change in slip systems from {111} to {100} planes, and there is no hardening associated with the {100} slip in the $L1_2$ structure.

Ni_3Al is capable of being hardened by solid-solution effects because it can dissolve substantial alloying additions without losing its long-range order. Figure 6 also shows the yield strength characteristics of an advanced aluminide containing 1.5 atom percent hafnium. Note a significant enhancement of strength properties and a displacement of peak strength to about 850°C in the case illustrated. The strengthening is entirely a result of solid-solution effects; no precipitates could be detected by transmission electron microscopy. Figure 7 compares the density-compensated ultimate tensile strength of Ni_3Al-based aluminide with that of commercial wrought alloys, including Waspaloy (one of the strongest nickel-based wrought superalloys in use). The comparison clearly indicates the superior strength-to-weight ratio of the aluminides (boron-doped Ni_3Al plus 0.5 to 1.0 atom percent hafnium) in both well-annealed and cold-worked conditions. Because of their aluminum content, the aluminides have a density about 10 percent less than that of nickel-base superalloys. The lower density could provide considerable advantages in applications involving rotating or moving parts.

Limited creep testing indicates that Ni_3Al exhibits grain-boundary sliding and [illegible] at 760°C. Alloying with

hafnium substantially lowers the creep rate and extends the creep life of the aluminides. Under the same test conditions, the creep rates of the aluminides are comparable to those of Waspaloy and are lower than those of Hastelloy X and type 316 stainless steel by two to three orders of magnitude. The alloys $(Fe,Co,Ni)_3V$ also exhibit excellent creep resistance (*14*). The formation of long-range order in these alloys lowers the creep rates by two orders of magnitude, apparently as a result of low atomic mobility in the ordered lattice.

At present, only limited fatigue and crack growth data exist for ordered intermetallic alloys. Stoloff and co-workers (*55*, *56*) recently found that ordered $(Fe,Ni)_3(V,Ti)$ alloys have good fatigue resistance, even though the alloys show a tendency for intergranular crack propagation at elevated temperatures. The superior fatigue properties of ordered alloys may be related to their planar slip behavior, which lowers the probability of crack nucleation and reduces the strain accumulation at crack tips because of increased slip reversibility. Comparison of the crack growth of an $(Fe,Ni)_3(V,Ti)$ alloy (LRO-60) with that of commercial superalloys showed crack growth for the ordered alloy to be distinctly slower than for superalloys in low stress intensity ranges Δk (*55*). The threshold Δk for the ordered alloy was higher than that for superalloys by a factor of about 3 to 4, indicating its superior resistance to crack growth.

The aluminide alloys based on Ni_3Al exhibit superior oxidation resistance in air at elevated temperatures because they are capable of forming adherent aluminum oxide films, which protect the base metal from excessive oxidation. The base aluminide, Ni_3Al, undergoes some spalling above 900°C; however, the spalling is easily suppressed by hafnium additions, which apparently improve the adhesion between the base metal and oxide film. Samples of the aluminide alloy Ni + 23 percent Al + 1 percent Hf and Hastelloy X were subjected to cyclic oxidation in air for 500 hours at 1100°C. In the oxidizing atmosphere a compact, adherent, protective film of oxide formed on the aluminide surface. In contrast, the Hastelloy X sample exhibited severe spalling, bulging, and wrinkling, presumably due to the combined effects of extensive oxidation and oxidation-induced internal stresses. The aluminide alloys truly represent a new series of high-temperature structural alloys that do not depend on chromium, a critical strategic element, for oxidation resistance.

Summary and Remarks

Ordered intermetallic alloys are a unique class of metallic alloys that have superior high-temperature properties; however, low ductility and brittle fracture restrict their use for structural applications. Recent studies have shown that the ductility and fabricability of ordered intermetallic alloys can be substantially improved by alloying processes and control of microstructural features through rapid solidification and thermomechanical treatments. These results demonstrate that the brittleness problem associated with ordered intermetallics can be overcome by using physical metallurgical principles.

Both macroalloying and microalloying have been proving very effective in improving the ductility and fabricability of several ordered intermetallic alloys. The ordered crystal structure in the Ni_3V-Co_3V-Fe_3V system can be systematically varied by change of electron concentration, *e/a*, and alloy composition. Through control of *e/a* by macroalloying (*13*, *14*) the $L1_2$-type ordered cubic structure is stabilized in $(Co,Fe)_3V$, $(Ni,Co,Fe)_3V$, and $(Ni,Fe)_3V$ alloys, which have excellent ductility and strength. Nickel aluminides based on Ni_3Al, having the ordered cubic structure, are ductile as single crystals but are extremely brittle in polycrystalline forms. The brittleness of such crystals is associated with a grain-boundary weakness that causes brittle intergranular fracture without appreciable plastic deformation within the grains. Microalloying studies (*15*, *16*, *19*, *20*) have shown that the ductility and fabricability of the aluminides can be dramatically improved by adding a few hundred parts per million of boron, which strongly segregates to the grain boundaries and improves their cohesion.

Success in alloy design has recently stimulated considerable interest in the development of ordered intermetallic alloys. Major efforts have been concentrated on aluminides based on Ni_3Al, Fe_3Al, Ti_3Al, NiAl, FeAl, and TiAl. These aluminides are particularly attractive because of their good corrosion resistance, low density, and relatively low cost. The aluminides based on Ni_3Al have greater yield strengths than cast superalloys above 800°C. The density of TiAl is 3.9 g/cm, compared with 8.2 to 9.0 for nickel-base superalloys. The density-compensated creep strength of TiAl is better than that of the cast superalloy IN-100 at temperatures to 1100°C (*57*). The most recent work of Vedula *et al.* (*58*) indicates that NiAl alloyed with a few percent niobium is also more creep resistant than IN-100 at 1200°C. All these results point to the development and use of aluminides for high-temperature structural applications.

At present, academic institutions, laboratories, and industry are making a joint effort to study ordered intermetallics. Academic study has focused on understanding the deformation, fatigue, and creep behavior of intermetallics; the government laboratories on mechanistic modeling, technology development, and property improvement; and industry on fabrication, alloy scale-up, and structural evaluation. The National Materials Advisory Board of the National Research Council has recently completed an assessment of ductile ordered intermetallic alloys for structural applications, which is expected to further stimulate both academic and industrial research on this new class of high-temperature materials.

References and Notes

1. N. S. Stoloff and R. G. Davies, *Prog. Mater. Sci.* 13 (No. 1), 1 (1966).
2. B. H. Kear, C. T. Sims, N. S. Stoloff, J. H. Westbrook, Eds., *Ordered Alloys—Structural Applications and Physical Metallurgy, Proceedings of the 3rd Bolton Landing Conference, September 1969* (Claitor's, Baton Rouge, La., 1970).
3. J. H. Westbrook, *Mechanical Properties of Intermetallic Compounds* (Wiley, New York, 1959).
4. ———, Ed., *Intermetallic Compounds* (Wiley, New York, 1967).
5. S. Takeuchi and E. Kuramoto, *Acta Metall.* **21**, 415 (1973).
6. P. H. Thornton, R. G. Davies, T. L. Johnston, *Metall. Trans.* **1**, 207 (1970).
7. S. M. Copley and B. H. Kear, *Trans. Metall. Soc. AIME* **239**, 977 (1967).
8. D. P. Pope, *Philos. Mag.* **25**, 917 (1972).
9. E. A. Aitken, in *Intermetallic Compounds*, J. H. Westbrook, Ed. (Wiley, New York, 1967), pp. 491–516.
10. L. E. Tanner *et al.*, *Mechanical Behavior of Intermetallic Compounds* (Report AST-TDR62-1087, Manlabs, Inc., Cambridge, Mass., 1963–1964), parts 1–3.
11. H. A. Lipsitt, D. Schechtman, R. E. Schafrik, *Metall. Trans. A* **11A**, 1369 (1980).
12. K. Aoki and O. Izumi, *Acta. Metall.* **27**, 807 (1979).
13. C. T. Liu and H. Inouye, *Metall. Trans. A* **10A**, 1515 (1979).
14. C. T. Liu, *Int. Metall. Rev.* **29**, 168 (1984).
15. K. Aoki and O. Izumi, *Nippon Kinzoku Takkaishi* **43**, 1190 (1979).
16. C. T. Liu and C. C. Koch, in *Proceedings of a Public Workshop on Trends in Critical Materials Requirements for Steels of the Future; Conservation and Substitution Technology for Chromium* (NBSIR-83-2679-2, National Bureau of Standards, Washington, D.C., June 1983).
17. E. M. Schulson and D. R. Barker, *Scr. Metall.* **17**, 519 (1983).
18. A. Inoue, H. Tomioku, T. Masumoto, *Metall. Trans. A* **14A**, 1367 (1983).
19. C. T. Liu, C. L. White, C. C. Koch, E. H. Lee, in *High Temperature Materials Chemistry—II*, L. A. Munir and D. Cubicciotti, Eds. (Electrochemical Society, Pennington, N.J., 1983), vol. 83, No. 7, pp. 32–41.
20. A. I. Taub, S. C. Huang, K. M. Chang, *Metall. Trans. A* **15A**, 399 (1984).
21. M. G. Mendiratta, S. K. Ehlers, D. K. Chatterjee, H. A. Lipsitt, in *Rapid Solidification Processing. Principles and Technologies III*, R. Mehrabian, Ed. (National Bureau of Standards, Washington, D.C., 1983), p. 240.
22. M. J. Marcinkowski, M. E. Taylor, F. X. Kayser, *J. Mater. Sci.* **10**, 406 (1975).
23. E. M. Grala, in *Mechanical Properties of Intermetallic Compounds*, J. H. Westbrook, Ed.

24. H. A. Lipsitt, O. Schechtman, R. E. Schafrik, *Metall. Trans. A* 6A, 991 (1975).
25. K. Aoki and O. Izumi, *Trans. Jpn. Inst. Met.* 19, 203 (1978).
26. C. T. Liu, C. L. White, J. A. Horton, *Acta Metall.*, in press.
27. W. C. Johnson *et al.*, *Scr. Metall.* 8, 971 (1974).
28. A. U. Seybolt and J. H. Westbrook, *Acta Metall.* 12, 449 (1964).
29. J. H. Westbrook and D. L. Wood, *J. Inst. Met.* 91, 174 (1962–63).
30. M. J. Marcinkowski, in *Order-Disorder Transformation in Alloys*, H. Warlimont, Ed. (Springer-Verlag, New York, 1974), pp. 364–403.
31. C. C. Koch, J. A. Horton, C. T. Liu, O. B. Cavin, J. O. Scarbrough, in *Rapid Solidification Processing, Principles and Technologies III*, R. Mehrabian, Ed. (National Bureau of Standards, Washington, D.C., 1983), pp. 264–69.
32. E. R. Slaughter and D. K. Das, in *Rapid Solidification Processing Principles and Technologies II*, R. Mehrabian, B. H. Kear, M. Cohen, Eds. (Claitor's, Baton Rouge, La., 1980), pp. 354–363.
33. N. S. Stoloff and I. L. Dillamore, in *Proceedings of the 3rd Bolton Landing Conference, September 1969* (Claitor's, Baton Rouge, La., 1970), p. 525.
34. J. D. Whittenberger, *Mater. Sci. Eng.* 57, 77 (1983).
35. J. Stefani and C. T. Liu, unpublished results.
36. P. A. Beck, *Adv. X-ray Anal.* 12, 1 (1969).
37. A. K. Sinha, *Trans. Metall. Soc. AIME* 245, 911 (1969).
38. S. Saito, *Acta Crystallogr.* 12, 500 (1959).
39. A. E. Dwight and P. A. Beck, *Trans. Metall. Soc. AIME* 215, 976 (1959).
40. J. H. N. VanVucht and K. H. Buschow, *J. Less-Common Met.* 10, 98 (1965).
41. J. H. N. VanVucht, *ibid.* 11, 308 (1966).
42. In these studies a third variable, the electrochemical affinity between atomic species, is maintained constant and therefore exerts no influence on ordered crystal structures.
43. A. K. Sinha, *Prog. Mater. Sci.* 15 (No. 2), 81 (1972).
44. D. F. Stein and L. A. Hedt, in *Interfacial Segregation*, W. C. Johnson and J. M. Brakely, Eds. (American Society of Metals, Metals Park, Ohio, 1977), pp. 239–260.
45. C. L. White and D. F. Stein, *Metall. Trans. A* 9A, 13 (1978).
46. C. L. Briant and R. P. Messmer, *Philos. Mag.* B-12, 569 (1980).
47. R. P. Messmer and C. L. Briant, *Acta Metall.* 30, 457 (1982).
48. A. I. Taub, S. C. Huang, K. M. Chang, General Electric Corporate Research and Development, private communications.
49. C. L. White, R. A. Padgett, C. T. Liu, S. M. Yalisove, *Ser. Metall.*, in press.
50. J. R. Rice, in *The Effect of Hydrogen on the Behavior of Metals* (American Institute of Mechanical Engineers, New York, 1976), pp. 455–466.
51. B. H. Kear, *Acta Metall.* 12, 555 (1964).
52. ——— and H. G. Wilsdorf, *Trans. AIME* 224, 382 (1962).
53. D. P. Pope and S. S. Ezz, *Int. Met. Rev.* 29, 136 (1984).
54. J. A. Horton and C. T. Liu, in preparation.
55. S. Ashok, K. Kain, J. M. Tartaglia, N. S. Stoloff, *Metall. Trans. A* 14A, 1997 (1983).
56. A. K. Kuruvilla and N. S. Stoloff, in preparation.
57. F. L. Versynder and M. Gell, in *Fundamental Aspects of Structural Alloy Design*, R. I. Jaffee and B. A. Wilcox, Eds. (Plenum, New York, 1977), pp. 209–227.
58. K. Vedula, G. Anderson, I. Aslanidis, *J. Met.* 35 (No. 12), 98 (1983).

59. We thank C. L. White, C. B. Finch, and A. DasGupta for useful comments on this manuscript. Thanks are also due to C. Dowker for preparation of the manuscript. Research sponsored jointly by the Division of Energy Conversion and Utilization Technologies (ECUT), the Division of Materials Sciences, and the AR & TD Fossil Energy Materials Program, U.S. Department of Energy, under contract No. DE-AC05-84OR21400 with Martin Marietta Energy Systems, Inc.

Ordered alloys

Physical metallurgy and mechanical properties of ductile ordered alloys $(Fe, Co, Ni)_3V$*

C. T. Liu

The physical metallurgy and mechanical properties of long-range ordered (LRO) alloys based on the quasiternary system Fe_3V–Co_3V–Ni_3V are reviewed comprehensively. Ordered crystal structures in $(Fe, Co, Ni)_3V$ alloys are characterized by specific sequences of stacked close-packed ordered layers, and their stacking character can be altered systematically by controlling the electron concentration (e/a) of the alloys. As e/a decreases, the stacking character changes from purely hexagonal, through different, ordered mixtures of hexagonal and cubic layers, to purely cubic. Partial substitution of Fe for Co and Ni lowers e/a, thus stabilizing the $L1_2$-type cubic ordered structure. Alloys with hexagonal ordered structures exhibit brittle fracture and very little ductility, but alloys with the cubic ordered structure are ductile. The mechanical behaviour of these ductile LRO alloys is reviewed, with emphasis on deformation at high temperatures. Unlike conventional solid-solution strengthened alloys, the yield strengths of the LRO alloys increase with temperature, peaking around the critical ordering temperature T_c (650–950°C). Further investigation suggests that this anomalous temperature dependence is caused by a thermally activated process, rather than a disordering process. The creep behaviour of the LRO alloys can be described by a power-law rate equation. All the alloys exhibit a discontinuous change in the steady-state creep rate in the vicinity of T_c, and the formation of LRO lowers it by two orders of magnitude. Other metallurgical and mechanical properties of the LRO alloys are also discussed, including workability, fatigue behaviour, hydrogen embrittlement, oxidation and corrosion, irradiation effects, and microstructural features. The review emphasizes the correlation of these properties with metallurgical variables in these alloys. The potential development of $(Fe, Co, Ni)_3V$ alloys as new structural materials for high-temperature applications is also discussed.

IMR/132

1. INTRODUCTION

Ordered alloys are a unique class of metallic materials, which form a long-range ordered (LRO) crystal structure below their critical ordering temperature T_c. Ordered alloys offer potential advantages over conventional, disordered alloys for high-temperature structural applications.[1–4] This superior performance can be attributed to the relatively low atomic mobility and unique dislocation dynamics of ordered lattices. The strength of ordered alloys does not degrade very rapidly with increasing temperature: for many such alloys, the yield strength shows an increase, rather than a decrease, with increasing temperature.[5–9] LRO produces stronger binding and closer packing between atoms. The restricted atomic mobility in ordered lattices generally results in slower diffusion processes and better creep resistance.

In spite of the above advantages, development of ordered alloys for high-temperature uses has met with only limited success.[10–14] The major difficulty with this class of alloys is their reported brittle fracture and low ductility, particularly at lower temperatures. The low fracture toughness can be related to two major metallurgical factors:

(i) low-symmetry ordered crystal structures having a limited number of slip systems[15]

(ii) grain-boundary embrittlement, primarily caused by segregation of harmful impurities.[16,17]

The former problem has recently been overcome by controlling the ordered crystal structure in Co_3V through 'macroalloying' processes.[18–21] This ordered structure can be altered systematically by partially replacing cobalt with nickel and iron. The beneficial effects of alloying with iron are to lower the electron concentration (e/a) (the number of valence electrons per atom) in the alloys and to stabilize the ordered crystal structure with the $L1_2$-type cubic stacking character. Such ordered alloys are ductile, with tensile elongations exceeding 35% at room temperature. Furthermore, by adjusting e/a, a series of cubic ordered alloys with compositions $(Fe, Co)_3V$, $(Fe, Co, Ni)_3V$, and $(Fe, Ni)_3V$ have been developed.

Dr C. T. Liu is with the Metals and Ceramics Division, Oak Ridge National Laboratory, Oak Ridge, Tenn., USA.

*Research sponsored by the Office of Energy Systems Research, Division of Energy Conversion and Utilization Technologies, US Department of Energy, Washington, DC, under contract W–7405–eng–26 with the Union Carbide Corp.

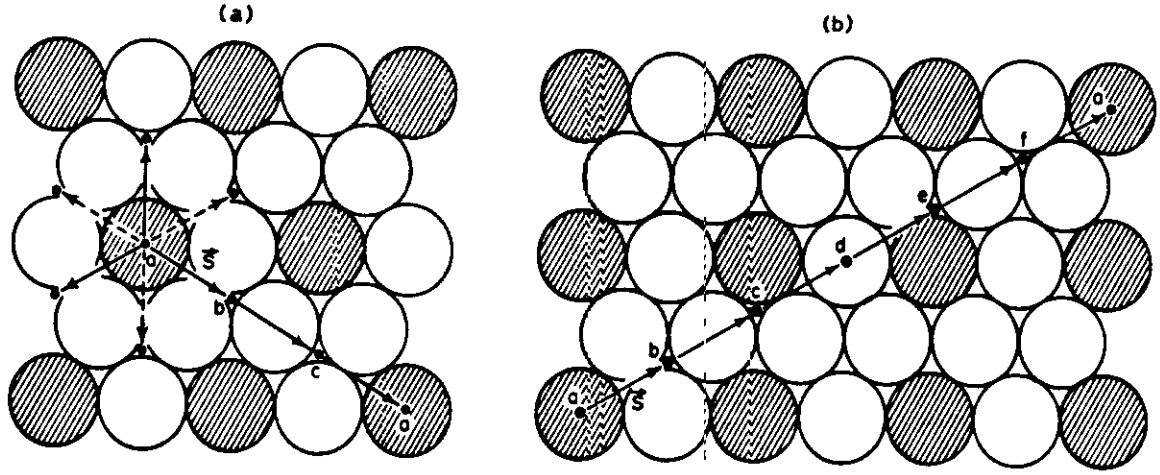

a triangular-type ordered layer; *b* rectangular-type ordered layer

1 Atomic structure on close-packed ordered planes; from Beck[22]

All these alloys are ductile and workable with promising high-temperature properties.

This paper provides a comprehensive review of the physical metallurgy and mechanical properties of the newly developed ordered alloys based on $(Fe, Co, Ni)_3V$.* Properties, including the crystal structure, tensile properties, creep behaviour, fatigue life, irradiation resistance, hydrogen embrittlement, and oxidation and corrosion behaviour of the ordered alloys are summarized and discussed, with emphasis on their correlation with metallurgical variables in the alloys. The potential development of $(Fe, Co, Ni)_3V$ alloys as new structural materials for high-temperature applications is also discussed.

2. EXPERIMENTAL ALLOYS: MICROSTRUCTURE AND PHASE RELATIONSHIPS

2.1 Influence of alloy variables on crystal structure in ordered A_3B alloys

In recent years, many close-packed, ordered structures have been observed in binary and multicomponent alloy systems with A_3B compositions.[22–30] All these structures are built up from the close-packed A_3B layer (Fig. 1*a*), but differ in their stacking sequence. Some of the ordered crystal structures have been reported to contain as many as 15 layers in a unit cell.[26] The ordered structure can best be rationalized by considering the character of each layer in a stacking sequence. A layer is characterized as hexagonal if its adjacent layers have the same stacking position. For example, with a stacking sequence ...ABA..., the layer B is classified as a hexagonal layer. On the other hand, the layer B is a cubic layer in a stacking sequence ...ABC..., in which its adjacent layers have different stacking positions.

A systematic study of close-packed, ordered A_3B structures has shown that the stacking character in many pseudobinary alloys can be correlated with two alloy variables — atomic-radius ratio (R_A/R_B) and electron concentration (e/a). Van Vucht and Buschow[26] and Van Vucht[27] have noted a general correlation between stacking character and R_A/R_B: as R_A/R_B decreases in A_3B ordered alloys, the stacking character changes from purely cubic, through different, ordered mixtures of cubic and hexagonal layers, to purely hexagonal. This change in stacking character can be rationalized from a consideration of packing density. The decrease in R_A/R_B allows clustering of the smaller A atoms and leads to the formation of open space (holes) in the layer (Fig. 2*a*). The larger B atoms in the adjacent layers are able to fit into the open spaces, thus producing a higher packing density (Fig. 2*b*). Note that the adjustment of atoms on the close-packed plane to give dense packing for the hexagonal crystal is at the expense of the cubic symmetry of the crystal.

Beck[22] and Dwight and Beck,[31] on the other hand, correlated the stacking character with e/a (defined as the average number of valence electrons per atom). With an increase in e/a, the ordered structure changes from predominantly cubic to predominantly hexagonal in character. A further increase in e/a also causes a change in the basic layer structure from a triangular type (Fig. 1*a*) to a rectangular type (Fig. 1*b*). The electron effect may originate from the interaction of the electron-concentration-dependent Fermi surface with the Brillouin zone.[32] Since the electron band structures of most ordered alloys are not known at the present time, it is almost impossible to treat the correlation quantitatively.

These correlations provide a very useful guide for predicting ordered crystal structures in A_3B compounds. An adjustment of alloy composition by partial replacement of A or B atoms with C atoms generally alters both R_A/R_B and e/a. There is no ambiguity in predicting the ordered crystal structure in the new alloys if both factors favour the change. However, it becomes difficult to predict the ordered structure when a change in one factor counteracts a change in the other; the stacking character in $(A, C)_3B$ or $A_3(B, C)$ must then be determined experimentally.

*In a broad sense, the alloy system $(Fe, Co, Ni)_3V$ includes the other two alloy systems, $(Fe, Co)_3V$ and $(Fe, Ni)_3V$.

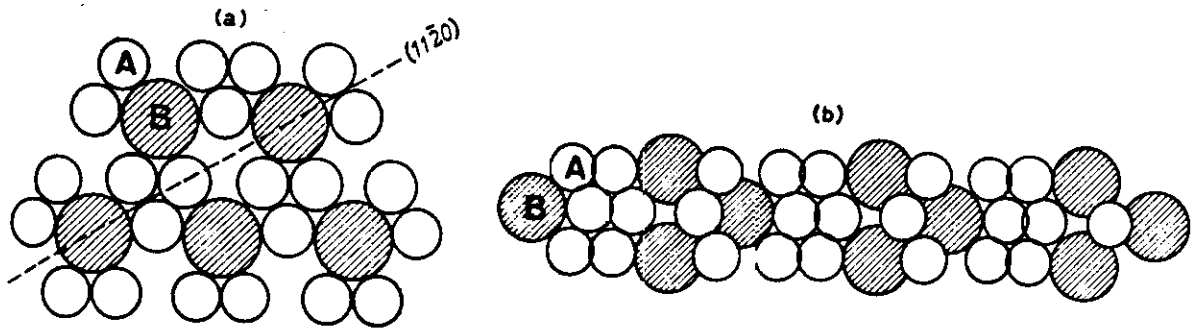

a clustering of smaller A atoms in hexagonal ordered basal layer; *b* projection of basal layers on (11$\bar{2}$0) plane; larger B atoms fit into holes formed by clustering shown in *a*

2 Change in packing pattern on change in atomic-radius ratio; from van Vucht[27]

2.2 Control of ordered crystal structures in Fe_3V–Co_3V–Ni_3V alloy systems

The ordered crystal structures of the binary alloys Ni_3V, Co_3V, and Fe_3V are given in Table 1, together with their e/a and R_A/R_B values. The alloys Ni_3V and Co_3V form tetragonal and hexagonal ordered structures, respectively, below their critical ordering temperatures T_C. It is not clear whether a LRO crystal structure exists in Fe_3V, because the retention of σ-phase in Fe_3V at high temperatures prevents the formation of the ordered structure at lower temperatures. In addition, T_C, if it exists, may be so low (~350°C) that ordering is extremely sluggish. The elements Ni, Co, and Fe have almost the same electronegativity and atomic size, but differ in e/a, having values of 10, 9, and 8, respectively. Thus, $(Fe, Co, Ni)_3V$ alloys provide an ideal basis from which to study the effect of e/a on close-packed, ordered crystal structure. Furthermore, these are transition metal alloys in which e/a should play a dominant role in determining the stability of various ordered structures.

Figure 3 summarizes the data available on the ordered crystal structures observed in the pseudobinary systems Ni_3V–Co_3V and Co_3V–Fe_3V (Refs. 18, 21, 23, 27). The binary alloy Co_3V forms a six-layered hexagonal ordered structure[33] with a stacking sequence ...ABCACB... (stacking character ...hcchcc ..., where h represents a hexagonal layer and c a cubic one). The hexagonality of the ordered structure is 33.3%. The e/a ratio in the alloy can be increased by partially replacing Co with Ni, producing $(Co, Ni)_3V$. With the resulting increase in e/a, the hexagonality of the ordered structure changes step by step from 33.3% to 66.7%, and finally to 100%. On the other hand, e/a in Co_3V can be lowered by partial substitution of Fe for Co to give $(Fe, Co)_3V$. For $e/a < 7.89$, the $L1_2$-type cubic ordered structure having the stacking sequence ...ABC... (...ccc...) is stabilized in $(Fe, Co)_3V$ alloys. All these results agree well with the prediction from Beck's correlation[22] based on the e/a effect.

To demonstrate anew the effect of e/a on ordered crystal structures, a portion of the cobalt atoms in $(Fe, Co)_3V$ can be replaced with equal numbers of nickel and iron atoms.[18–20] This scheme alters the alloy composition, but not the e/a value of the alloy. As indicated in Fig. 4, the cubic ordered structure remains stable in $(Fe, Co, Ni)_3V$ alloys that have the same e/a value as $(Fe, Co)_3V$. Eventually, when all the cobalt atoms are replaced with nickel and iron atoms, one obtains cubic ordered alloys having the compositions $(Fe, Ni)_3V$. Using this scheme the $L1_2$-type cubic ordered structure may be stabilized in $(Fe, Ni)_3V$ alloys, alloys that do not contain Co, an expensive, strategic element.

2.3 Alloy preparation and fabrication

The cubic ordered ($L1_2$-type) alloys with compositions $(Fe, Co, Ni)_3V$ were prepared by arc or electron-beam melting and drop casting into a 25 × 13 × 140 mm rectangular mould. To minimize the impurity content in the alloys, electron-beam

Table 1 Crystal structures, critical ordering temperatures T_C, electron concentrations (e/a), and atomic-radius ratios (R_A/R_B) of A_3B-type binary alloys Ni_3V, Co_3V, and Fe_3V

	Ni_3V	Co_3V	Fe_3V
Ordered crystal structure	Tetragonal $D0_{22}$ or *I*18	Hexagonal hP24	...
T_C, °C	1045	1070	...
Basic layer structure	Rectangular	Triangular	...
e/a*	8.75	8.00	7.25
R_A/R_B†	0.930	0.936	0.942

*Defined as number of valence electrons per atom.
†Atomic-radius ratios of A and B atoms in A_3B compositions; calculated from Pauling radii for coordination number 12.

ALLOY	Ni_3V	$(Co,Ni)_3V$	$(Co,Ni)_3V$	Co_3V	$(Co,Fe)_3V$	Fe_3V
e/a	8.75	8.54	8.43	8.00	<7.89	7.25
ORDERED LAYER	R	T	T	T	T	
STACKING SEQUENCE		AB	ABCBCACAB	ABCACB	ABC	
STACKING CHARACTER		hh	hchhchhch	hcchcc	ccc	
HEXAGONALITY (%)		100	66.7	33.3	0	

3 Effect of electron concentration (e/a), defined as number of valence electrons per atom, on ordered structures in Ni_3V–Co_3V and Co_3V–Fe_3V pseudobinary systems;[18,21,23,27,33] R represents rectangular ordered layer, T triangular, *see* Fig. 1

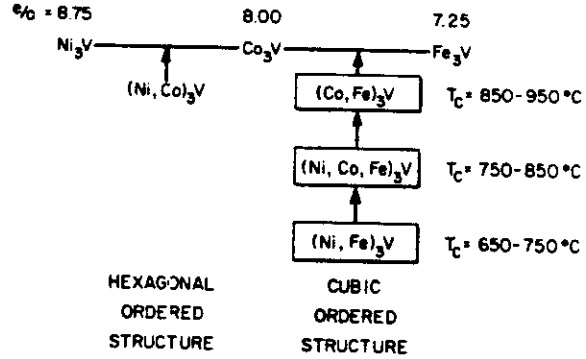

4 Stabilization of $L1_2$ cubic ordered structure through control of electron concentration (e/a) in $(Fe,Co,Ni)_3V$ alloys

melted Fe, Co, and Ni, and high-purity V (total impurity level <700 ppm) were used as charge materials. The sheet fabrication involves hot rolling ingots between molybdenum cover sheets at 1100°C, followed by cold rolling at room temperature. The molybdenum cover sheets were used for thermal insulation and preventing excessive oxidation. After hot breakdown, the alloy plates were cold rolled to a reduction in thickness of 40–60% without difficulty. The as-rolled sheets were of good quality, with no indication of surface or end cracks (Fig. 5). In comparison, the Co_3V alloy, with its hexagonal ordered crystal structure, cracked badly during hot rolling at 1100°C (Fig. 5). The results given in Table 2 show good agreement between nominal and analysed alloy compositions. The final sheets usually contained <600 ppm total interstitial impurities, mainly oxygen, carbon, and nitrogen.

The cubic ordered alloys also have good formability. Hardware such as hemishells and capsules can readily be formed at room temperature. Figure 6 shows thin-wall capsules fabricated by cold forming and electron-beam welding. The ordered alloys were basically weldable by both arc and electron-beam welding processes. David *et al.*[34] are currently attempting to characterize the welding behaviour and fusion-zone microstructures of these ordered alloys.

Ordered alloys with base composition $(Fe,Co,Ni)_3V$ were modified with <1%Ti to improve their ductility at elevated temperatures. Titanium was added as a partial replacement for vanadium; that is, the modified alloys have the alloy formula $(Fe,Co,Ni)_3(V,Ti)$. Table 3 lists the nominal alloy compositions of the cubic ordered alloys, designated as LRO alloys, whose properties are discussed in this paper.

Commercial-grade, impure ferrovanadium was used to lower the alloy production cost. Such material contains 80–85%V, 12–15%Fe, 1–4%O, and <2%Al+Si. A titanium-modified alloy, LRO-37 ($(Fe_{50}Ni_{50})_3(V_{98}Ti_2)$), was prepared from both pure vanadium and ferrovanadium. The properties of the heats prepared from the ferrovanadium were comparable to those of the heats from the pure vanadium, indicating that no adverse effects arise from using ferrovanadium as the feed material.

2.4 Phase relationships

The phase relationships in base and titanium-modified LRO alloys were determined[18–20] by quenching and aging in the temperature range

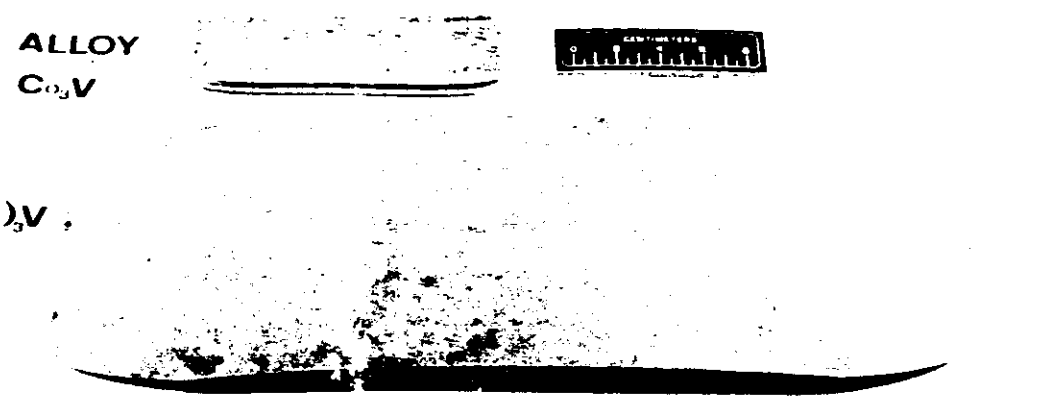

5 Comparison of formabilities of cubic ordered alloy $(Fe,Co,Ni)_3V$ and hexagonal ordered alloy Co_3V

Table 2 Alloy compositions and chemical analyses of experimental (Fe, Co, Ni)$_3$V alloys prepared by arc melting

Alloy	Alloy formula	Composition, at.-% Nominal				Analysed				Interstitial concentration,* wt-ppm			
		Fe	Co	Ni	V	Fe†	Co	Ni‡	V‡	O	C	N	H
LRO-5	$(Fe_{15}Co_{85})_3V$	11.3	63.7	0	25.0	11.8	bal.	0	24.9	118	114	144	<1
LRO-1	$(Fe_{22}Co_{78})_3V$	16.5	58.5	0	25.0	17.3	bal.	0	25.1	140	146	141	<1
LRO-2	$(Fe_{30}Co_{70})_3V$	22.5	52.5	0	25.0	22.6	bal.	0	24.9	142	198	155	<1
LRO-3	$(Fe_{33.3}Co_{66.7})_3V$	25.0	50.0	0	25.0	24.6	bal.	0	25.1	152	110	147	<1
LRO-4	$(Fe_{40}Co_{50}Ni_{10})_3V$	30.0	37.5	7.5	25.0	29.6	bal.	7.4	25.2	161	105	143	<1

*Determined by vacuum fusion and carbon analyses.
†Determined by volumetric method, accuracy ±2%.
‡Determined by atomic-absorption method, accuracy ±3%.

400–1200°C. Two types of phase relationship were observed in LRO alloys, the one observed depending on the alloy composition (Fig. 7). In the type-I phase relationship, the disordered solid solution γ transforms to the cubic ordered γ' ($L1_2$-type ordered crystal structure) below the critical ordering temperature T_c. The $\gamma \rightarrow \gamma'$ transformation involves only the ordering of atoms with respect to fcc lattice sites; that is, (V, Ti) atoms occupy corner sites and (Fe, Co, Ni) atoms occupy face-centred sites. In the type-II relationship, precipitation of σ-phase from the γ solid solution occurs at temperatures below T_1, and the two phases transform to the ordered γ' via the peritectoid reaction $\gamma + \sigma \rightarrow \gamma'$ below T_c. The σ-phase has a tetragonal crystal structure with $a = 0.885$ and $c = 0.459$ nm, values that agree well with the literature data for the σ-phase ($a = 0.88$–0.89, $c = 0.45$–0.46 nm) observed in the Fe–V and Co–V systems.[35,36]

Figure 8 shows the variation of T_c with iron concentration. The results shown were derived from X-ray-diffraction data and from measurements of thermal expansion and mechanical properties. The linear relation in Fig. 8 gives an average decrease in T_c of ~10 K/at.-%Fe. Extrapolation to 75%Fe indicates that T_c for Fe_3V, if it exists, is ~350°C.

The occurrence of σ-phase in LRO alloys appears to be dependent on e/a, which affects both T_c and T_1 (the peak temperature for precipitation of σ-phase). This is indicated in Fig. 9, in which T_c and T_1 are plotted against e/a for the $(Fe,Co)_3V$ and $(Fe,Ni)_3V$ alloy systems. The value of T_c increases steadily, while T_1 decreases sharply with increasing e/a; both these trends reduce the stability of the σ-phase in LRO alloys. The σ-phase eventually becomes unstable in LRO alloys as T_1 becomes equal to T_c. This observation generally agrees with the Phacomp scheme,[37,38] which has been developed, on the basis of electronic considerations, for the prediction of σ-phase formation in superalloys. The σ-phase is an electron compound;[32] its stability is largely affected by e/a. According to the Phacomp scheme, the γ solid solution becomes unstable and starts

Table 3 Nominal compositions of LRO alloys

Alloy	Nominal alloy formula	Alloy composition, at.-%					Alloy composition, wt-%				
		Fe	Co	Ni	V	Ti	Fe	Co	Ni	V	Ti
LRO-1	$(Fe_{22}Co_{78})_3V$	16.5	58.5	0	25.0	0	16.3	61.1	0	22.6	0
LRO-2	$(Fe_{30}Co_{70})_3V$	22.5	52.5	0	25.0	0	22.3	55.0	0	22.7	0
LRO-3	$(Fe_{33.3}Co_{66.7})_3V$	25.0	50.0	0	25.0	0	24.8	52.5	0	22.7	0
LRO-4	$(Fe_{40}Co_{50}Ni_{10})_3V$	30.0	37.5	7.5	25.0	0	29.9	39.5	7.9	22.7	0
LRO-5	$(Fe_{15}Co_{85})_3V$	11.3	63.7	0	25.0	0	11.1	66.4	0	22.5	0
LRO-15	$(Fe_{48}Co_{27}Ni_{25})_3V$	36.0	20.3	18.7	25.0	0	36.0	21.4	19.8	22.8	0
LRO-16	$(Fe_{61}Ni_{39})_3V$	45.7	0	29.3	25.0	0	46.1	0	31.0	22.9	0
LRO-17	$(Fe_{52}Co_{10}Ni_{38})_3V$	39.0	7.5	28.5	25.0	0	39.1	7.9	30.1	22.9	0
LRO-20	$(Fe_{50}Ni_{50})_3V$	37.5	0	37.5	25.0	0	37.6	0	39.5	22.9	0
LRO-23	$(Fe_{22}Co_{78})_3(V_{96}Ti_4)$	16.5	58.5	0	24.0	1.0	16.4	61.1	0	21.7	0.8
LRO-34	$(Fe_{22}Co_{78})_3(V_{98.2}Ti_{1.8})$	16.5	58.5	0	24.5	0.5	16.3	61.1	0	22.2	0.4
LRO-35	$(Fe_{60}Ni_{40})_3(V_{98.2}Ti_{1.8})$	45.0	0	30.0	24.5	0.5	45.3	0	31.8	22.5	0.4
LRO-37	$(Fe_{50}Ni_{50})_3(V_{98}Ti_2)$	37.5	0	37.5	24.5	0.5	37.6	0	39.5	22.4	0.4
LRO-38	$(Fe_{50}Ni_{50})_3(V_{96}Ti_4)$	37.5	0	37.5	24.0	1.0	37.6	0	39.5	22.0	0.9
LRO-39	$(Fe_{60}Ni_{40})_3(V_{96}Ti_4)$	45.0	0	30.0	24.0	1.0	45.3	0	31.8	22.0	0.9
LRO-41	$(Fe_{55}Ni_{45})_3(V_{96}Ti_4)$	41.3	0	33.7	24.0	1.0	41.5	0	35.6	22.0	0.9
LRO-42*	$(Fe_{50}Ni_{50})_3(V_{98}Ti_2)$	37.5	0	37.5	24.5	0.5	37.6	0	39.5	22.4	0.4

*A small quantity of rare earth elements was added to this alloy.

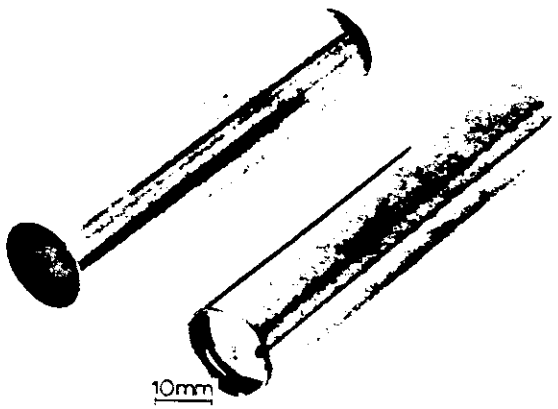

6 **Thin-walled capsules made from cubic ordered (Fe,Co,Ni)$_3$V alloys**

to precipitate the σ-phase when e/a is below a critical value (or, say, when a critical electron vacancy number is exceeded). Figure 9 shows that σ-phase is completely suppressed as a stable phase in LRO alloys when e/a exceeds 7.79 in (Fe, Co)$_3$V and 8.01 in (Fe, Ni)$_3$V alloys.

The grain structures of LRO-20 in the ordered and disordered states are compared in Fig. 10. The disordered grain structure was produced by quenching from 1150°C, and the ordered structure was obtained by annealing the quenched specimen at a temperature below T_C. Ordering apparently does not change grain structure, implying that no nucleation of new grains occurs during ordering processes. Numerous twins are observed in the LRO alloys, their number generally increasing with increasing cobalt concentration. The precipitation morphology of σ-phase in LRO alloys depends on annealing temperature and alloy composition. In general, blocky σ particles precipitate on grain boundaries at high temperatures (Fig. 11*a*), but finer particles precipitate along crystallographic planes at lower temperatures, producing a Widmanstätten-type structure (Fig. 11*b*).

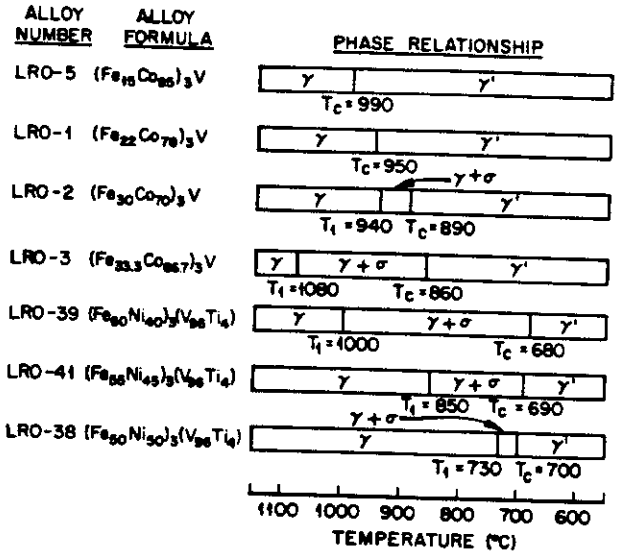

7 **Phase relationships in base and Ti-modified LRO alloys**

2.5 Structural features

Structural features of LRO alloys in the ordered and disordered states have been studied.[18,39] Both X-ray-diffraction and mechanical-property measurements indicate that the disorder → order transformation can be suppressed by water quenching from temperatures above T_C. However, for the alloys with higher values of T_C, such as LRO-1 with T_C = 950°C, the disordered state can be retained only in thin-section specimens (<1mm). Some degree of short-range order probably existed in the as-quenched LRO-1 alloy, since selected-area diffraction (SAD) patterns showed diffuse intensity in the {100} superlattice positions.[39]

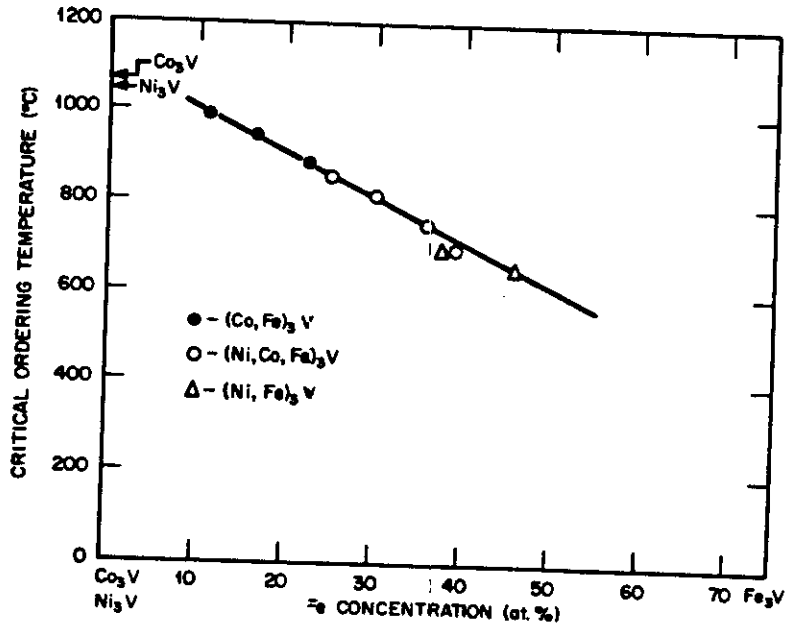

8 **Critical ordering temperature T_C as function of Fe concentration present in (Fe,Co,Ni)$_3$V alloys**

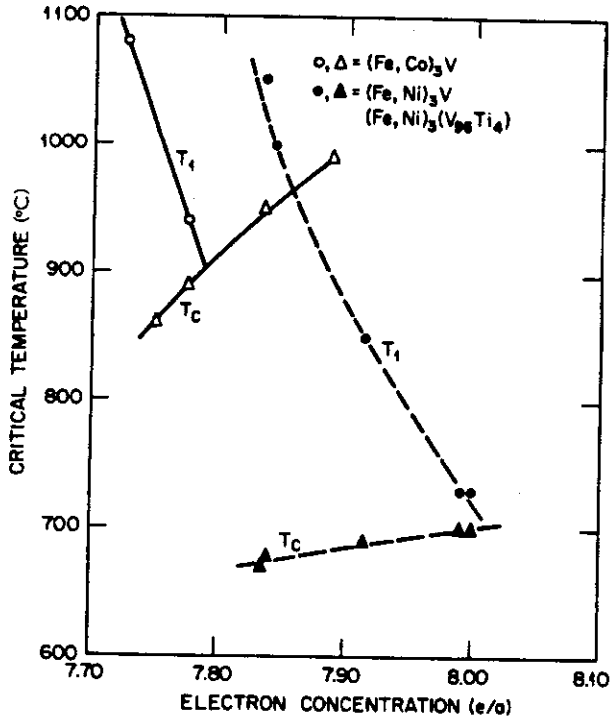

9 Variation of critical ordering temperature T_C and peak temperature for σ-phase precipitation T_1 with electron concentration (e/a)

Carbide-precipitation, antiphase-boundary (APB), and domain structure were studied quite extensively by transmission electron microscopy (TEM) in LRO-1 alloy.[39] Small VC-type particles distributed uniformly in the matrix were observed in as-quenched specimens. When quenched specimens were aged at 700°C, VC precipitated, initially discontinuously on grain boundaries, and later on extrinsic stacking faults in the matrix. Figure 12 shows the cellular structure formed by the migration of a high-angle boundary into adjacent grains, with narrow strings of VC trailing behind. The driving force for cell formation can derive from the discontinuous-precipitation reaction, coarsening of domain structures, or both. 'Recrystallized' cells without precipitation have been observed during the aging of other ordered alloys,[40] and their formation is solely derived from the coarsening of domain structures. Aging at 800°C produced blocky VC particles at grain boundaries, with fine VC precipitation on extrinsic stacking faults, but not on intrinsic stacking faults. There was no evidence of any discontinuous precipitation at 800°C.

Numerous intrinsic and extrinsic stacking faults were observed in the ordered specimens produced by aging at 800°C. By a careful contrast analysis, Braski *et al.*[39] identified the modes of nucleation for both types of stacking fault. Extrinsic stacking faults were nucleated at VC particles by the punching out of perfect dislocations, which dissociated into Frank and Shockley partials as follows:

$$(a/2)[011] \rightarrow (a/6)[\bar{2}11] + (a/3)[111]$$

The Frank partial climbed away from the particle, and growth of the stacking fault proceeded by the Silcock–Tunstall mechanism[41] of alternate precipitation and climb of the Frank partial. Intrinsic stacking faults were also nucleated at VC particles, but the perfect dislocation around the particle dissociated into two Shockley partials:

$$(a/2)[\bar{1}01] \rightarrow (a/6)[\bar{1}\bar{1}2] + (a/6)[\bar{2}11]$$

The intrinsic fault then grew by glide of the outer Shockley partial.

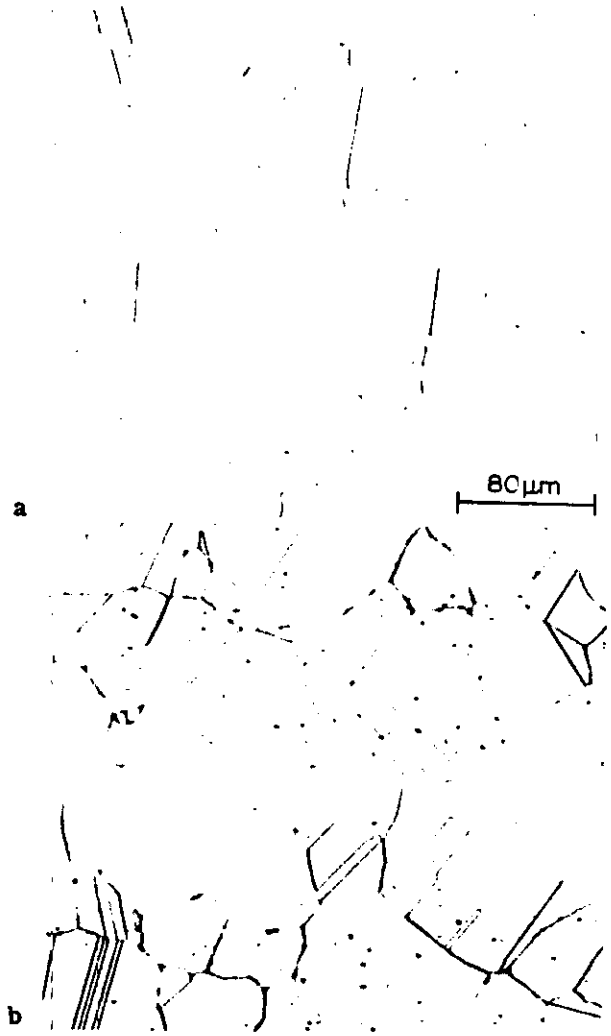

a disordered state produced by quenching from 1150°C; *b* ordered state produced by aging quenched specimen at 550–650°C

10 Microstructure of LRO-20 in ordered and disordered states

The stacking faults were generally observed in ordered samples, but not in disordered ones. This suggests that the faults are more stable in the ordered state. The stability of the stacking faults in the ordered state can be rationalized by considering fault energies in (Fe,Co)$_3$V alloys. First, the formation of LRO may lower the stacking-fault energy, as observed by Cockayne *et al.*[42] in Cu_3Au. They found that the fault energy in ordered Cu_3Au (13.0 MJm^{-2}) is 40% smaller than that in disordered Cu_3Au (21.5 MJm^{-2}). Second, the low stacking-fault energy in LRO-1 can be rationalized from the stability of ordered crystal structures in (Fe, Co)$_3$V alloys, the stacking sequence of which can readily be altered by small changes in cobalt concentration. For instance, an extrinsic

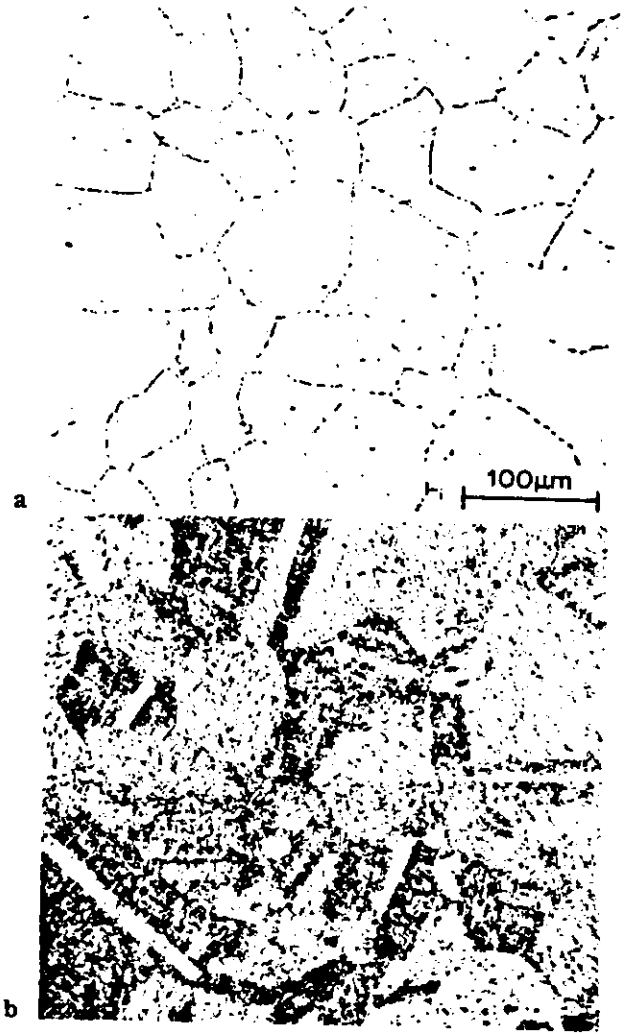

a annealed 1 h at 950°C; *b* annealed 500 h at 725°C

11 Morphology of σ-phase precipitation in LRO-39 after different heat treatments

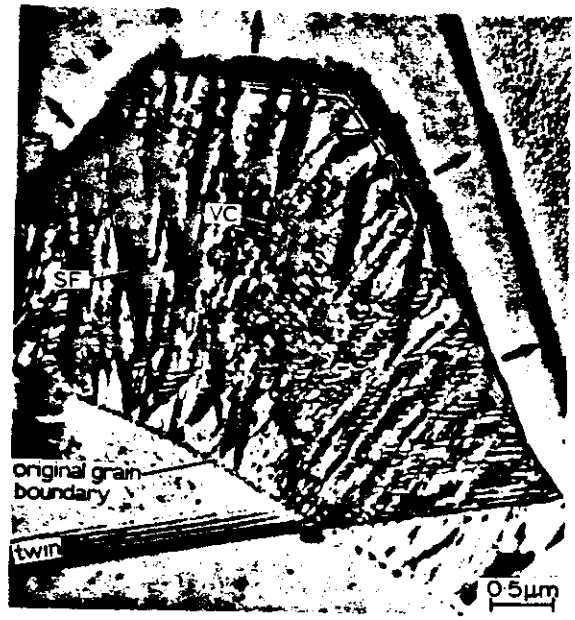

12 Discontinuous precipitation of VC associated with 'cells' formed by migration of high-angle boundary into adjacent grains with narrow strings of VC trailing behind; from Braski *et al.*[39]

stacking fault alters the stacking sequence in the $L1_2$ ordered structure from ...ABCABC... to ...ABCA|C|B...; the latter is the stable ordered structure in Co_3V. It is thus expected that the stacking faults will be quite stable in the $(Fe_{22}Co_{78})_3V$ alloy, because of its low stacking-fault energy.

The domain structures in $(Fe, Co)_3V$ and $(Fe, Ni)_3V$ can readily be revealed by using dark-field superlattice reflections.[39] Figure 13 shows the growth of ordered domains in LRO-1 alloy at 700°C. The domain boundaries appear wavy,

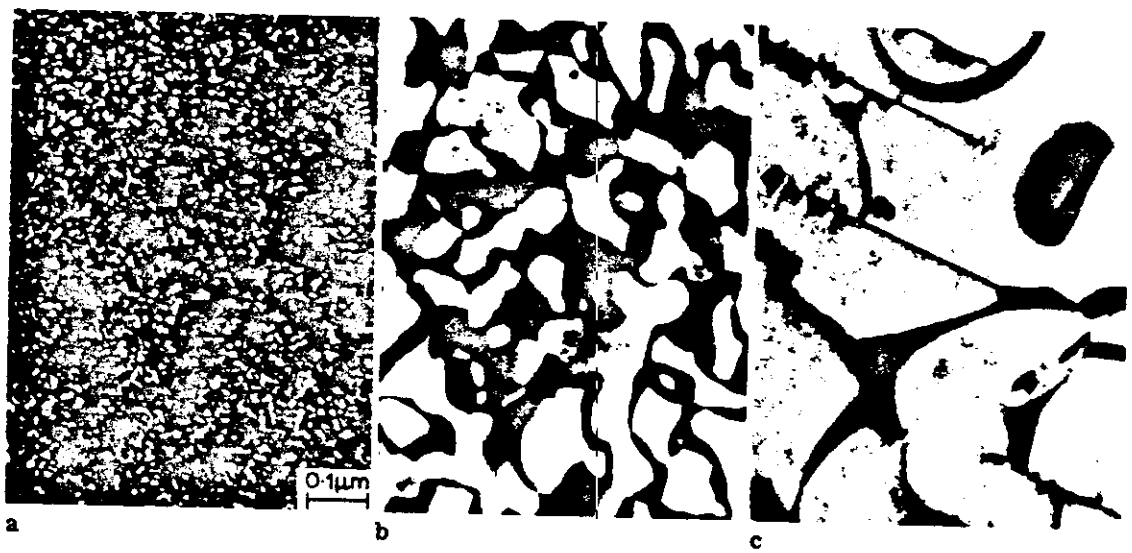

a 1 h; *b* 16.7 h; *c* 266.7 h

13 Superlattice dark-field micrographs showing growth of ordered domains in LRO-1 after annealing at 700°C for various times; from Braski *et al.*[39]

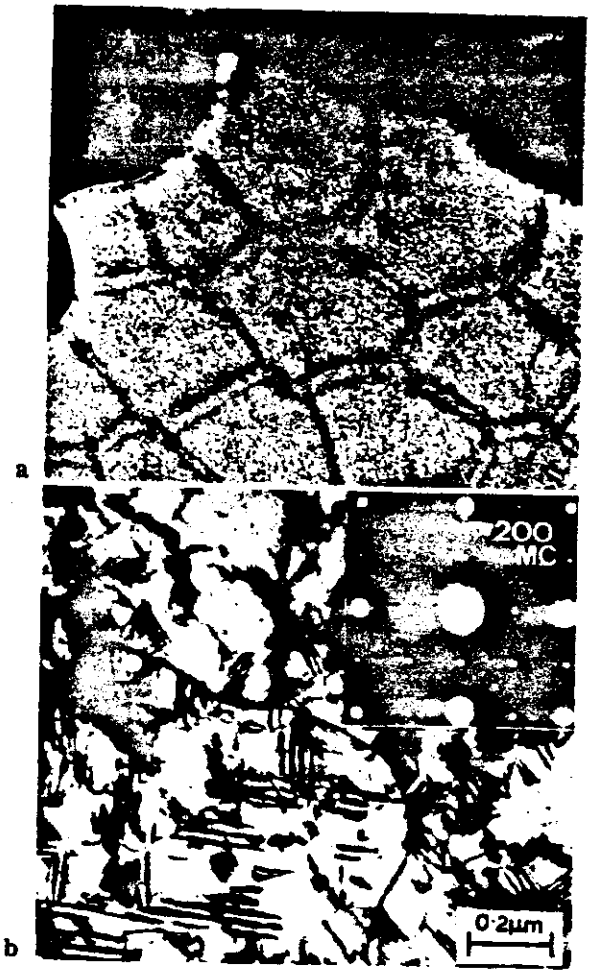

a as-quenched specimen, showing cellular structure; *b* rapidly solidified and annealed specimen, showing extensive stacking faults

14 Bright-field micrographs of rapidly solidified LRO-1; from Lee *et al.*[49]

indicating that the APB energy is quite isotropic in LRO-1. Wavy boundaries have been observed in other $L1_2$ ordered alloys, such as Ni_3Mn, Ni_3Fe, and Cu_2NiZn (Refs. 43–46). The domain structures in these ordered alloys are different from the maze-pattern domains found in Cu_3Au, in which the APBs show a strong tendency to lie on cube planes.[47] Braski *et al.*[39] found that ordered domains in LRO-1 grew according to the equation

$$d = \alpha t^{1/2} \exp(-Q/RT) \quad . \quad . \quad . \quad . \quad . \quad (1)$$

where d is the domain diameter, α a constant, t the aging time at 700–900°C, and Q the apparent activation energy for domain growth. The activation energy Q was measured as 222 kJmol^{-1}, which is much smaller than the value (393 kJmol^{-1}) obtained from creep tests on the same alloy.[48]

Dislocation structures have not been studied extensively in LRO alloys. Observations on APBs in LRO alloys strongly suggest that superlattice dislocations in these alloys are composed of two unit dislocations connected by a piece of APB, rather than two superpartials connected by a stacking fault. Of course, the unit dislocations are expected to dissociate fully into Shockley partials, because of the relatively low stacking-fault energy in LRO alloys.

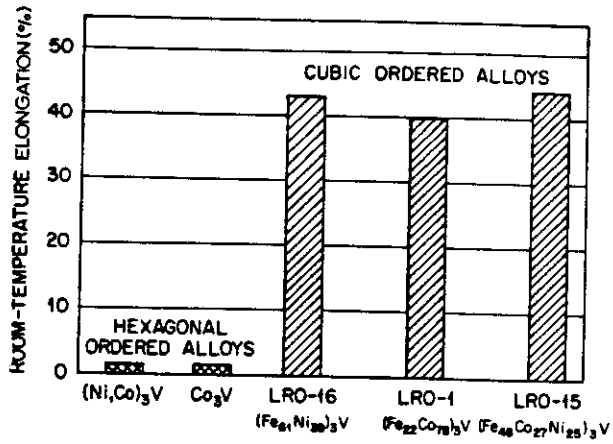

15 Comparison of room-temperature tensile elongations of cubic and hexagonal alloys

2.6 Rapidly solidified LRO alloys

The influence of rapid-solidification processing on the microstructure of LRO-1 and LRO-37 was studied by TEM.[49] Rapid solidification was accomplished by an arc-hammer technique with an estimated cooling rate of 5×10^6 Ks^{-1}. The rapid solidification did not suppress crystallization; instead, it produced a disordered fcc crystal structure with a fine (~2 μm diameter) grain size. The main structural feature of the as-quenched alloys was a fine (~300 nm diameter) hexagonal cell structure decorated with carbide particles (Fig. 14*a*). SAD indicated that the VC particles were randomly oriented with respect to the matrix. Small cavities, probably formed by vacancy condensation, were also seen in the as-quenched samples along cell boundaries. The location of voids at the cell boundaries suggests a strong interaction between solute atoms and vacancies.

The cell structure remained after an ordering treatment of 5 h at 800°C followed by 17 h at 700°C, which indicated that recrystallization did not occur during the heat treatment. The VC particles in the cell boundaries exhibited a cube-on-cube orientation relationship with the matrix after annealing. A high density of stacking faults was observed in the ordered state (Fig. 14*b*). The voids observed in the as-quenched specimens disappeared during annealing.

3. MECHANICAL PROPERTIES

3.1 Tensile properties

Tensile properties of $(Fe, Co, Ni)_3V$ alloys have been characterized as a function of ordered crystal structure (cubic *v.* hexagonal), alloy composition, and test temperature.

3.1.1 Room-temperature ductility of cubic and hexagonal ordered alloys

Figure 15 compares the room-temperature elongations to failure of cubic and hexagonal ordered alloys. The ductility of these alloys

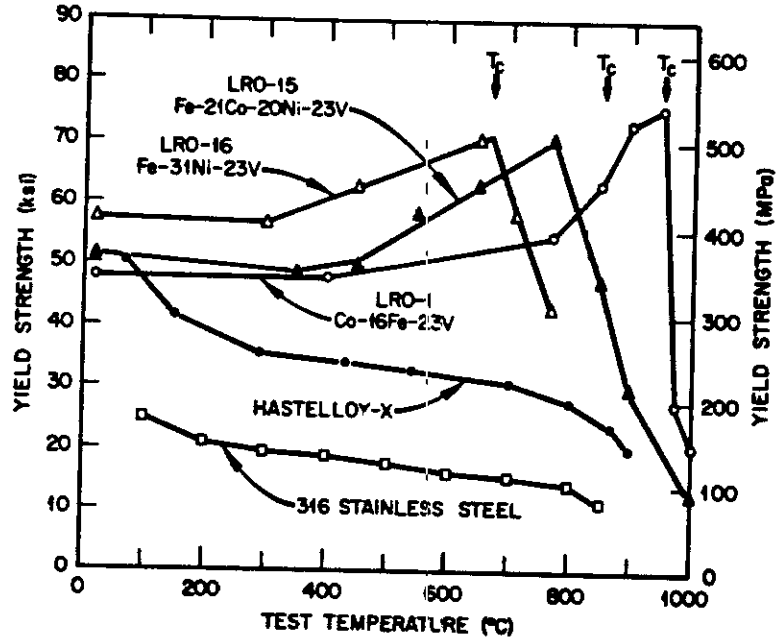

16 Variation of yield strength with test temperature for cubic ordered alloys and commercial solid-solution strengthened alloys Hastelloy-X and type 316 stainless steel

appears to be independent of alloy composition, but is sensitive to the ordered crystal structure.[18] The cubic ordered alloys LRO-1 ($(Fe_{22}Co_{78})_3V$), LRO-15 ($(Fe_{48}Co_{27}Ni_{25})_3V$), and LRO-16 ($(Fe_{61}Ni_{39})_3V$) are all ductile, showing tensile elongations exceeding 35%, but the hexagonal ordered alloys Co_3V and $(Ni, Co)_3V$ are extremely brittle (<1% elongation at room temperature). The deformation behaviour of the ductile, cubic ordered alloys is expected to be similar to that of fcc materials, which have 12 independent deformation systems, based on {111} slip. The brittleness of the hexagonal ordered alloys is mainly related to the limited number of slip systems available in the multilayered hexagonal ordered crystal structure. The change of the ordered crystal structure from cubic to hexagonal symmetry may lower the number of slip systems from 12 to 3 (corresponding to basal or prismatic slip). Furthermore, deformation by twinning would be difficult in the hexagonal ordered lattice because twinning causes local disordering.[50,51] The cubic → hexagonal transformation also significantly increases the lattice frictional stress, because of interplanar-locking effects (*see* Fig. 2*b*). This is manifested in the appreciable decrease in the lattice spacing along the *c*-axis during the cubic → hexagonal transformation in the $(Co_{43}Ni_{57})_3V$ alloy.[21]

The effect of the ordered structure on ductility was further demonstrated[21] by measurements of tensile elongation on the alloy $(Co_{43}Ni_{57})_3V$, in which both the cubic and hexagonal ordered structures were produced by aging treatments. The alloy was in the disordered condition following quenching from above T_c. Isothermal aging at subcritical temperatures, such as 700°C, resulted first in the formation of the cubic ordered γ' (a metastable phase) from the fcc disordered γ, and subsequently in transformation of the γ' to the nine-layered hexagonal ordered κ (a stable phase). Tensile tests indicated that the κ structure was extremely brittle, although the γ' was ductile, with a tensile elongation of 31% at room temperature.

In general, the ductility of the cubic ordered LRO alloys is insensitive to alloy composition for alloys containing up to 60 at.-%Co (Ref. 18). This is illustrated by the results in Fig. 15, all the cubic ordered LRO alloys being ductile with elongations >35%. The LRO alloys with up to 60 at.-%Co exhibited transgranular fracture surfaces of ductile-dimple-type appearance. However, the tendency for grain-boundary fracture to occur increases with increasing cobalt content beyond that level. The alloy containing 64 at.-%Co exhibited essentially grain-boundary fracture, showing an elongation of only 14%. The brittle fracture is thought to be associated with the segregation of harmful impurities (such as sulphur) to grain boundaries in the high-cobalt alloy.

3.1.2 Yield and tensile strengths of cubic ordered LRO alloys

The yield strengths σ_y of cubic ordered LRO alloys are shown in Fig. 16 as a function of temperature. The distinct feature of the plot is that the yield strengths of these LRO alloys increase with temperature, rather than decreasing, as do those of conventional disordered alloys such as Hastelloy X and type 316 stainless steel. The σ_y values for these LRO alloys increase substantially with temperature above 400°C, and reach a maximum around T_c. Because of the increase, the LRO alloys become much stronger than disordered solid-solution alloys at elevated temperatures. The strengths of the LRO alloys are lower than those of precipitation-strengthened superalloys such as Inconel 718 and Waspaloy, at lower temperatures, but comparable to or higher than them near T_c. For instance, in LRO-1 alloy σ_y reaches 520 MNm^{-2} at 900°C, a value markedly higher than those for Inconel 718 (300 MNm^{-2}) and Waspaloy

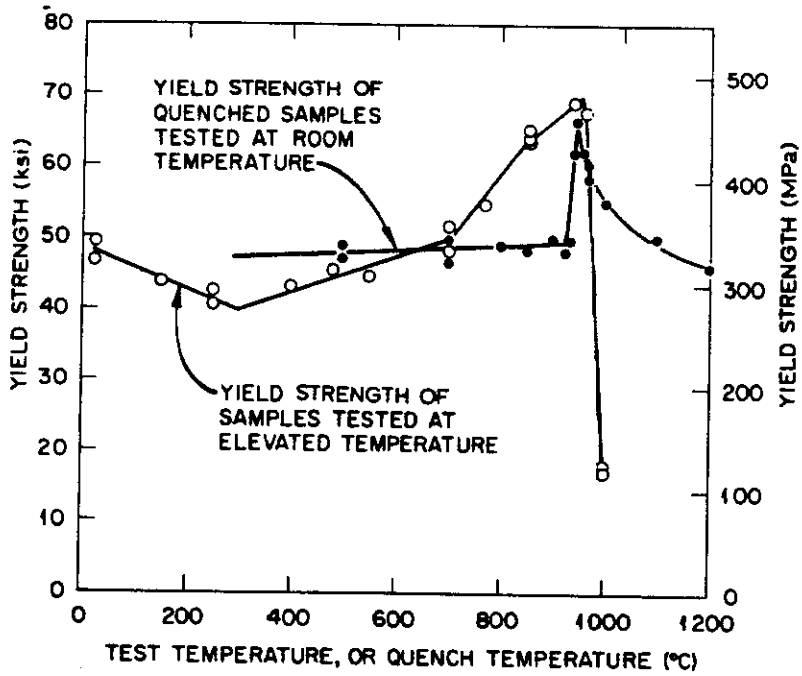

17 Variation of yield strength with test and quench temperature for LRO-1

(400 MNm^{-2}). The strength of the LRO alloys decreases sharply above T_c, apparently because of the loss of LRO. Thus, T_c represents an upper temperature limit for using LRO alloys.

An increase in σ_y with temperature has been observed in other $L1_2$ ordered alloys, such as Cu_3Au (Refs. 53–55), Ni_3Al (Refs. 5, 6, 56–58), Ni_3Ga (Refs. 59, 60), $Ni_3(Al, Nb)$ (Ref. 9), and $Ni_3(Al, W)$ (Ref. 61). Two types of mechanism have been proposed to explain the positive temperature dependence of the strength, based on thermally activated processes[5,59] and partial-disordering effects.[1,54] According to the solid-solution model proposed by Pope,[54] the increase in σ_y at high temperatures is caused by a modulus interaction between moving dislocations and local regions of disorder within the ordered matrix. As the temperature is raised, the LRO parameter decreases, and these regions become more numerous; σ_y therefore increases. On the other hand, Takeuchi and Kuramoto[59] have proposed that the anomalous temperature dependence of σ_y is caused by an increase in the number of sessile segments on dislocation lines cross-slipped on {111} planes. The sessile segments are formed by the cross-slip of one of the unit dislocations constituting a superdislocation from the {111} slip planes onto the {100} planes, in order to reduce the total energy of the dislocation. This cross-slip process was first suggested by Kear and Wilsdorf[62] to explain the high work-hardening rate observed in ordered alloys.

To identify which of the mechanisms was operating in LRO-1, σ_y was determined as a function of both test and quench temperature;[52] the results are shown in Fig. 17. For determining σ_y at high temperatures, ordered samples were held at temperature for 30–60 min before testing, the time depending on the test temperature. Neutron-diffraction studies indicated[63] that the partially ordered state could be retained to room temperature by water quenching. The samples tested at elevated temperatures start to show an increase in σ_y around 300°C, but the as-quenched samples tested at room temperature exhibit no significant increase until the quench temperature approaches T_c (950°C). This result strongly suggests that the positive temperature dependence of σ_y in LRO alloys is related to a thermally activated process, rather than a change in the degree of order caused by rising temperature. $\Delta\tau$, the shear-stress increment caused by the temperature effect,[52] is plotted as a function of T^{-1} in Fig. 18. The plot shows a linear relation between $\ln\Delta\tau$ and T^{-1}, indicating that $\Delta\tau$ is indeed produced by a thermally activated process. The apparent activation energy Q is measured as 4.8×10^{-20} J/atom (0.31 eV/atom), which is larger than for Ni_3Al (Refs. 6, 9) or Ni_3Ga (Ref. 60).

Pope[64] has recently determined the compressive yield stress of LRO-1 single crystals as a function of test temperature. Preliminary results indicate that all crystals with orientations near [110], [011], [$\bar{1}$11], and [$\bar{1}\bar{2}$3] show an increase in σ_y until close to T_c, above which σ_y dramatically decreases. However, σ_y does not appear to be strongly dependent on orientation, suggesting that the Takeuchi–Kuramoto cross-slip model may not provide a good explanation of the observed increase in yield stress. Further studies are therefore needed to elucidate the anomalous temperature dependence of σ_y in LRO alloys.

The as-quenched samples showed a sharp increase in room-temperature σ_y for quench temperatures in the vicinity of T_c (Fig. 17). This increase can be explained[1] on the basis of a transition from deformation by superlattice dislocations in the ordered state to deformation by unit dislocations in the disordered state. In other words, neither unit dislocations nor superlattice dislocations can glide easily through a structure

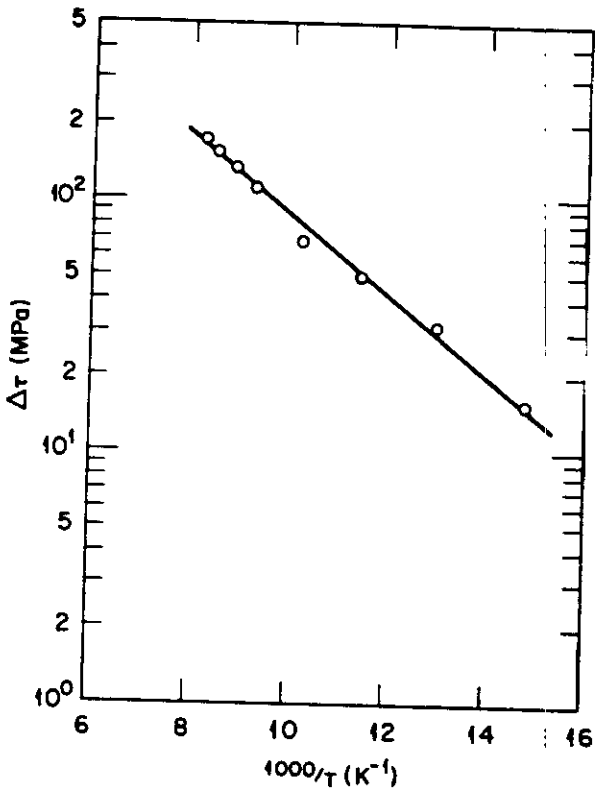

18 Variation of shear-stress increment caused by positive temperature dependence of yield strength $\Delta\tau$ with temperature T for LRO-1

in a weakly ordered or strongly short-range ordered state without encountering extra resistance.

The ultimate tensile strengths (UTS) as a function of test temperature for LRO-1, LRO-3, and LRO-4 are shown in Fig. 19. UTS appears to be insensitive to temperature up to 400°C, above which it decreases markedly. The decrease is apparently caused by recovery from strain hardening during the tests at elevated temperatures. The tensile strength of the LRO alloys is twice that of Hastelloy-X and three times that of type 316 stainless steel, at all the test temperatures.

3.1.3 *Effect of temperature on ductility and fracture behaviour*

The ductility and fracture behaviour of LRO alloys typically show three distinct features[65] when the alloys are deformed slowly at temperatures in the range 25–1000°C. Figure 20 shows the variation of tensile elongation of LRO-1 with temperature at strain rates of 3.3×10^{-3} and 42×10^{-3} s^{-1}. From 25 to 700°C, the elongations obtained ranged from 34 to 44%, fracture being by ductile shearing at 45° to the tensile axis (Fig. 21*a* and *b*). Microscopic examination of fracture surfaces indicated that the fracture processes involved the nucleation and growth of microvoids, followed, eventually, by their linkage via the shearing of the connecting ligaments of metal (Fig. 22*a* and *b*). A possible explanation of this fracture behaviour is that localized reduction in the degree of LRO on active slip planes reduces the work-hardening capacity, causing continuous slip along the weak planes, and leading to a final shear-off.

From 700 to 960°C, the ductility decreases gradually, reaching a minimum of 4% at T_c (Fig. 20). Correspondingly, the macroscopic failure surface changes its orientation to a plane at ~90° to the tensile axis (Fig. 21*c*), while the microscopic features become more intergranular (Fig. 22*c*). The gradual transition from transgranular ductile fracture at 700°C to intergranular brittle fracture around 960°C suggests that diffusion effects become important as the temperature increases over this range. As a result, voids nucleated at grain boundaries tend to grow rapidly because of high rates of diffusion along these boundaries. This type of intergranular fracture is expected to be suppressed by high-strain-rate deformation, as under these conditions the mass transport via vacancy migration becomes insignificant during the time of the test. Indeed, the

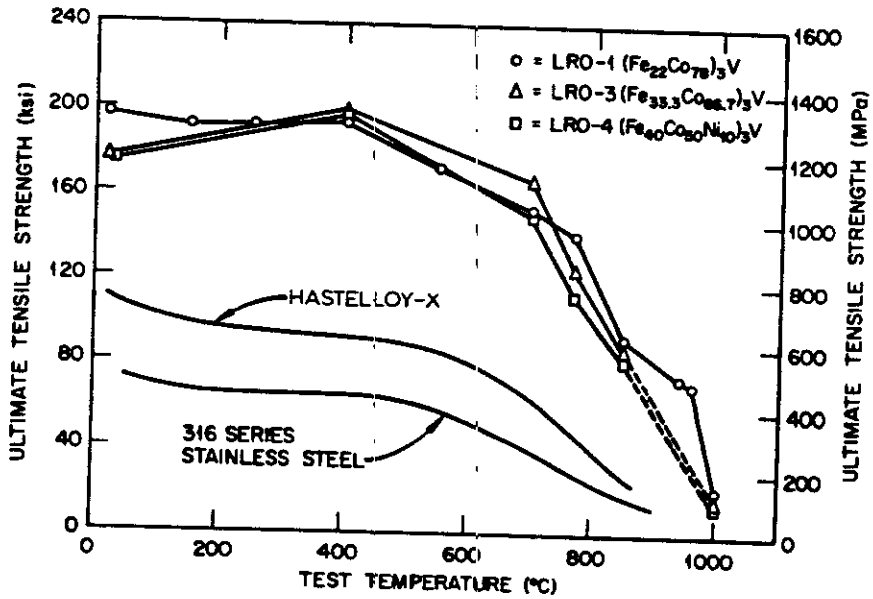

19 Ultimate tensile strength of various ordered alloys as function of test temperature

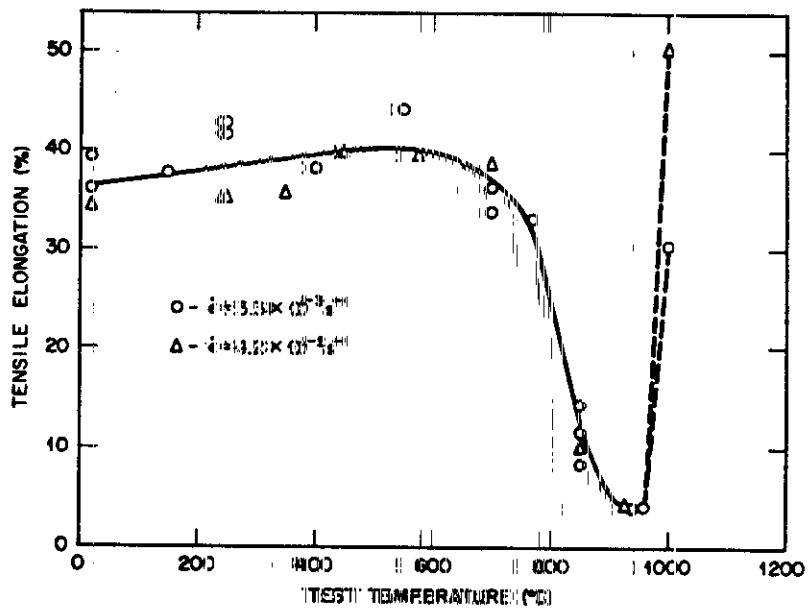

20 Variation of tensile elongation with test temperature and strain rate $\dot{\varepsilon}$ for LRO-1

author has found that a specimen tested at a high strain rate of 4.8×10^3 s^{-1} at 950°C showed an elongation of 52% and a fracture mode similar to that at lower temperatures.

From 960 to 1000°C, the ductility increases sharply, reaching 30% at the lower strain rate of 3.3×10^{-3} s^{-1} and 50% at the higher rate of 42×10^{-3} s^{-1} (Fig. 20). The marked increase in ductility is apparently a result of the order → disorder transformation, which sharply lowers the flow stresses (Fig. 16). At 1000°C, the macroscopic fracture surface is quite highly fragmented, although it is still generally perpendicular to the tensile axis (Fig. 21*d*). Microscopically, the surface is characterized by a bimodal distribution of granular features (Fig. 22*d*): coarse ones of a scale similar to the original grain size (~30 μm), together with fine ones closer to 1 μm in diameter. The fine nodules are believed to be individual grains produced by a dynamic recrystallization localized near grain boundaries (Fig. 20). Nodules with a similar appearance had been observed near grain boundaries during the high-temperature deformation of Zr_3Al, another $L1_2$ alloy.[66]

3.1.4 *Effect of minor alloy additions on tensile properties*

The LRO alloys exhibit a susceptibility to grain-boundary fracture and reduced ductility at temperatures above 700°C. The observed ductility minimum results from a combination of weak grain boundaries and a high flow stress at temperatures near T_c. In an attempt to improve the ductility at elevated temperatures, the LRO alloys were alloyed with up to 4% of reactive elements from Groups III to VI of the periodic table.[37] Of the elements added, the Group IVA elements (Ti, Zr, and Hf) were found to be most effective. Figure 24 shows plots of tensile properties as a function of temperature for examples of the base and titanium-modified LRO alloys.[7] The yield strengths of LRO-20 and LRO-37 increase with temperature, reaching peak values around T_c. Both alloys are ductile, with tensile elongations exceeding 35% below 450°C. Above 450°C, the ductility of the base alloy, LRO-20, decreases markedly with temperature and reaches a minimum of 14.6% near T_c. In comparison, the ductility of the titanium-modified LRO-37 depends on temperature to a much lesser extent, and shows only a moderate drop near T_c. The ductility minimum of LRO-37 is 28% at 700°C. Thus, modifying with Group IVA elements significantly improves the ductility of base LRO alloys at elevated temperatures. The beneficial effect of these elements is not well understood, but may be related to the gettering of harmful impurities (such as sulphur) segregated at grain boundaries. Titanium, hafnium, and zirconium have all been reported to be effective in improving the ductility of nickel-base alloys,[68] which are often embrittled by segregation of sulphur at grain boundaries. Additions of titanium also improve the creep ductility and fatigue resistance, as is discussed below.

LRO alloys were also prepared using commercial-grade ferrovanadium, thus lowering the material cost. The ferrovanadium contains a high level of impurities (O, C, Al, and Si), but can be purified to a certain extent by electron-beam melting. Figure 25 compares the tensile properties of LRO-37 prepared from high-purity vanadium (LRO-37), as-received ferrovanadium (LRO-37-5), and electron-beam-melted ferrovanadium (LRO-37-6).[67] For all the heats, σ_y increases with temperature, reaching a peak value around T_c. The values of T_c for the ferrovanadium heats appear to be slightly lower than that for the high-purity heat, presumably because the ferrovanadium heats are slightly off the stoichiometric composition, owing to the higher levels of impurities. The ferrovanadium heats exhibit distinctly higher yield strengths, these probably resulting from the combined hardening effect of a finer grain size (Fig. 26) and higher volume fractions of carbide and oxide

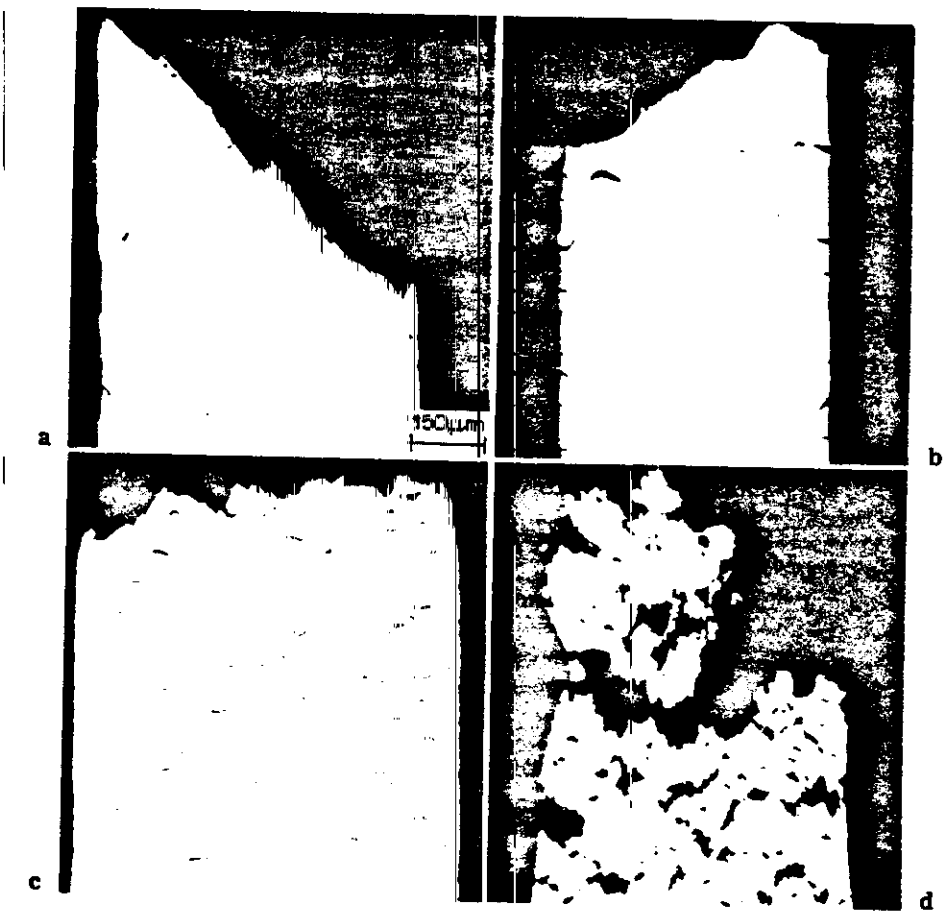

a room temperature; *b* 700°C; *c* 860°C; *d* 1000°C

21 **Macroscopic fracture features of LRO-1 tested in tension at various temperatures; from Liu and Schulson[65]**

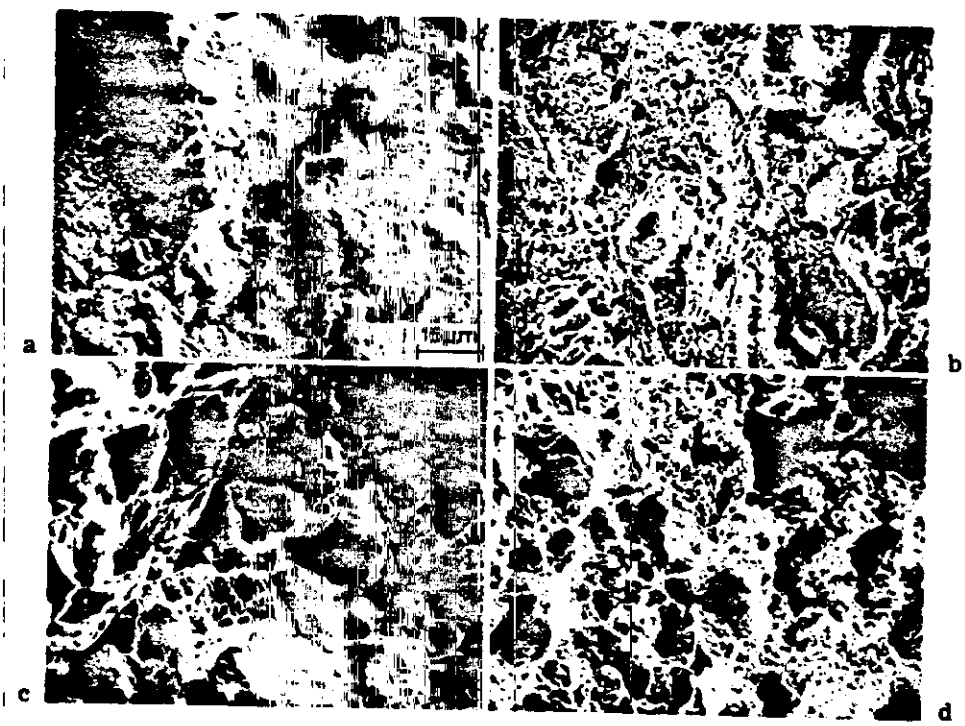

a room temperature; *b* 700°C; *c* 860°C; *d* 1000°C

22 **Microscopic fracture features of LRO-1 tested in tension at various temperatures; from Liu and Schulson[65]**

23 Surface cracks in LRO-1 specimen fractured in tension at 1000°C, showing nodules formed by dynamic crystallization localized along grain boundaries

precipitates in the LRO-37-5 and LRO-37-6 heats. The ferrovanadium heats were ductile; total tensile elongation exceeded 25% at all test temperatures. The elongations of the ferrovanadium heats were somewhat lower than that of the pure vanadium heat below 700°C; however, there is no major difference in ductility between them. The characterization of the tensile properties described above demonstrated that it is feasible to prepare the LRO alloys with ferrovanadium as a charge material.

3.2 Creep properties

Creep properties of LRO alloys were determined[20,48] as a function of the ordered state, test temperature, and applied stress in vacuum (1 mPa). Figure 27 shows semilog plots of steady-state creep rate $\dot{\epsilon}$ as a function of reciprocal temperature for the alloys LRO-1, LRO-2, and LRO-3. The creep tests were performed at 69 MNm^{-2} (10 ksi) in the temperature range 760–1000°C (>0.6T_m, where T_m is the alloy melting point). The creep data, independent of alloy composition, can be grouped into two curves, corresponding to the ordered and disordered states. Each alloy shows a rapid change in creep rate around T_c (865–950°C). Extrapolation of data from above T_c to below T_c reveals that formation of LRO lowers $\dot{\epsilon}$ by two orders of magnitude, as indicated by the dashed lines in Fig. 27. The discontinuous change in $\dot{\epsilon}$ at T_c has been observed in the iron-base LRO alloys[20] (Fe, Ni)$_3$V (Fig. 28), as well as in other $L1_2$ ordered alloys.[69]

In order to understand the creep behaviour, the creep data were analysed using the power-law rate equation[70] generally used for high-temperature creep (>0.5T_m)

$$\dot{\epsilon} = \alpha \frac{\sigma^n}{\mu^{n-1}T} \exp(-Q/RT) \quad . \quad . \quad . \quad . \quad (2)$$

where α is a materials constant, σ the applied stress, n the strain rate sensitivity exponent, μ the shear modulus, and Q the apparent activation energy for creep. The exponent n in the ordered state was measured as 4 on a log–log plot of $\dot{\epsilon}$ as

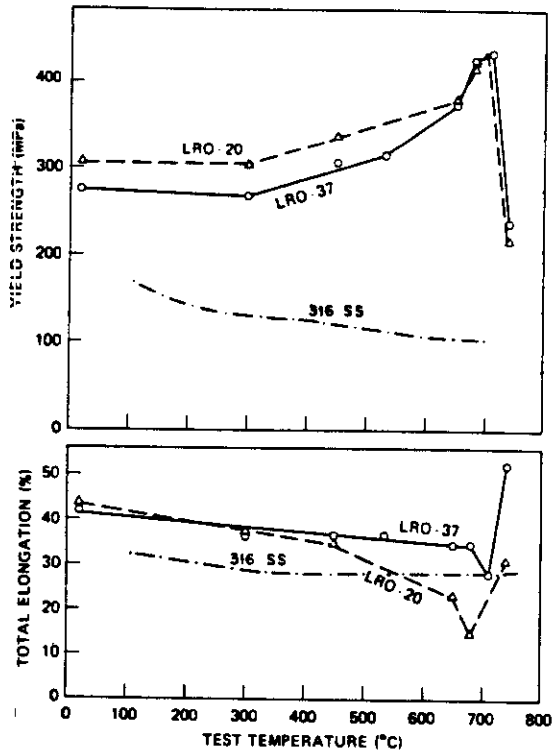

24 Variation of tensile yield strength and elongation with test temperature for base alloy LRO-20 and Ti-modified alloy LRO-37

a function of σ. The modulus $\mu(T)$ showed a rapid change in value at T_c, as determined from measurements of Young's modulus as a function of temperature.[52] Putting these parameters into equation (2) and rearranging gives

$$\dot{\epsilon}\mu^3 T = \alpha\sigma^4 \exp(-Q/RT) \quad . \quad . \quad . \quad . \quad (3)$$

The creep data in Fig. 27 are replotted in Fig. 29 according to equation (3). The plot also displays a change of two orders of magnitude in $\dot{\epsilon}\mu^3$ around T_c. Comparison of Figs. 27 and 29 indicates that this abrupt change is caused mainly by $\dot{\epsilon}$-related effects, rather than by μ-related ones. The values of Q measured from the slopes of the curves in Fig. 29 are equal to 393 and 356 kJmol^{-1} for the ordered and disordered states, respectively. Formation of LRO thus causes only a small increase in Q. In contrast, bcc ordered alloys, such as β-brass[71,72] and FeCo,[72,73] exhibit a large increase in Q (60–100%) upon ordering.

The discontinuous change in creep rate can result from either a sharp change in diffusivity or a change in creep mode during the order → disorder transformation. Further studies are required to determine the creep rate as a function of stress in the disordered condition; it will then be possible to assess the n value accurately in the disordered state and to compare the value obtained with that of n in the ordered state.

The creep rates of LRO alloys are compared with those of solid-solution alloys, such as Hastelloy X (Ref. 74) and type 316 stainless steel,[75] in Fig. 30. Under the same test conditions, the creep rates of the LRO alloys are lower than those

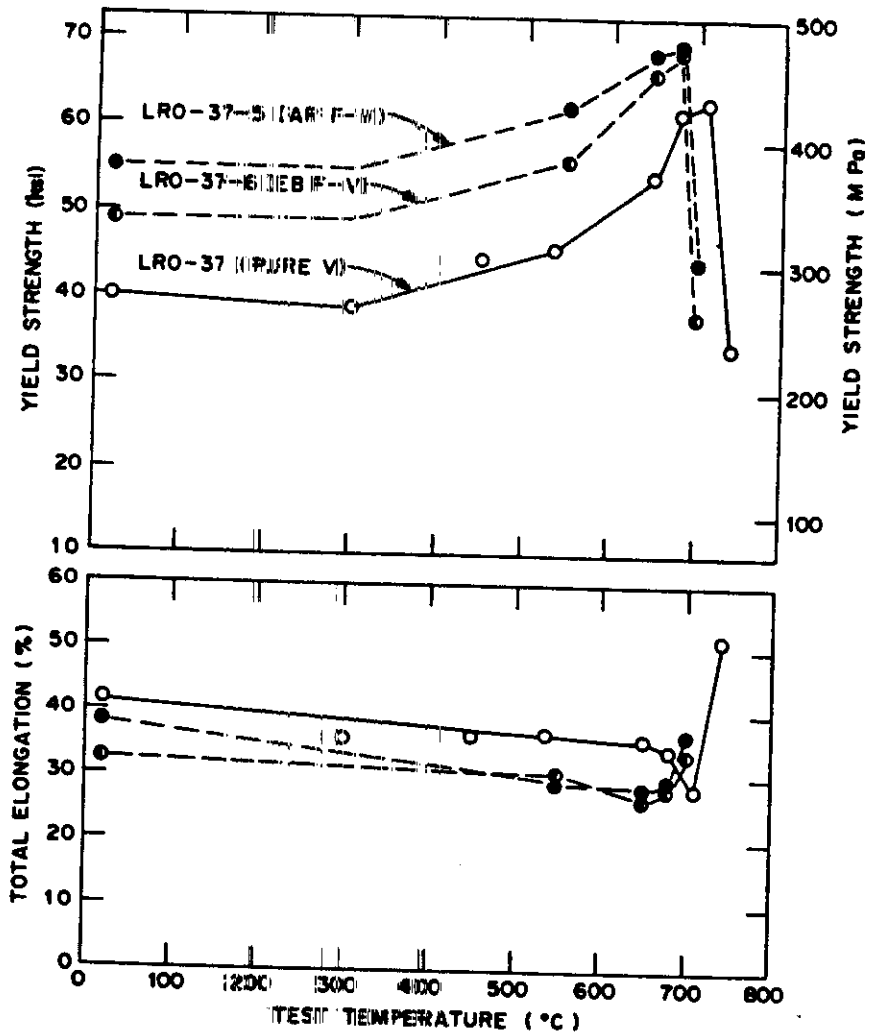

25 Variation of yield strength and elongation with test temperature for LRO-37 prepared from pure vanadium (LRO-37), electron-beam melted ferrovanadium (LRO-37-6), and as-received ferrovanadium (LRO-37-5); after Liu[67]

of the commercial alloys by about three orders of magnitude. The superior creep resistance of LRO alloys is mainly derived from LRO effects, which lower the creep rate by two orders of magnitude (Fig. 27). In comparison with particle-strengthened superalloys, the creep resistance of LRO alloys is better than that of Inconel 718 and comparable to that of Waspaloy.

The base alloys LRO-1, LRO-2, and LRO-3 exhibited rupture ductilities of <15% at temperatures below T_c. Microscopic examination of fractured surfaces revealed that this low ductility is associated with the nucleation, growth, and coalescence of cavities along grain boundaries. The creep ductility of the cobalt-base LRO alloys $(Fe, Co)_3V$ can be greatly improved by adding a small amount of titanium.[67] For example, alloy LRO-34, containing 0.5 at.-%Ti, showed ductile fracture with extensive necking (Fig. 31), and a rupture elongation of 52%. The suppression of grain-boundary failure is also believed to be aided by the gettering action of titanium additions, which prevents harmful impurities from segregating to grain boundaries. However, titanium additions have been found to have only a limited effect on improving the creep ductility of the iron-base LRO alloys $(Fe, Ni)_3V$. The present author[67] is currently working on further improving the creep ductility of $(Fe, Ni)_3V$ by alloying with rare earth elements, which have a very strong affinity for impurities such as sulphur and oxygen.

3.3 Fatigue properties

Fatigue properties of the base alloy LRO-1 ($(Fe_{22}Co_{78})_3V$), as well as the titanium-modified alloys LRO-23 ($(Fe_{22}Co_{78})_3(V_{96}Ti_4)$) and LRO-37 ($(Fe_{50}Ni_{50})_3(V_{98}Ti_2)$), were studied under load-controlled tension–tension fatigue tests.[76] All tests were conducted in vacuum at a minimum stress of 34.5 MNm^{-2} and a frequency of 20 Hz. The fatigue properties of the base alloy LRO-1 were quite sensitive to test temperature and showed considerable heat-to-heat variation. This behaviour may have resulted from a strong tendency toward grain-boundary fracture in base LRO alloys, as indicated by the change in the fatigue fracture mode in LRO-1, from transgranular at low temperatures to intergranular at high temperatures. The problem of grain-boundary fracture was alleviated by adding a small amount of titanium.

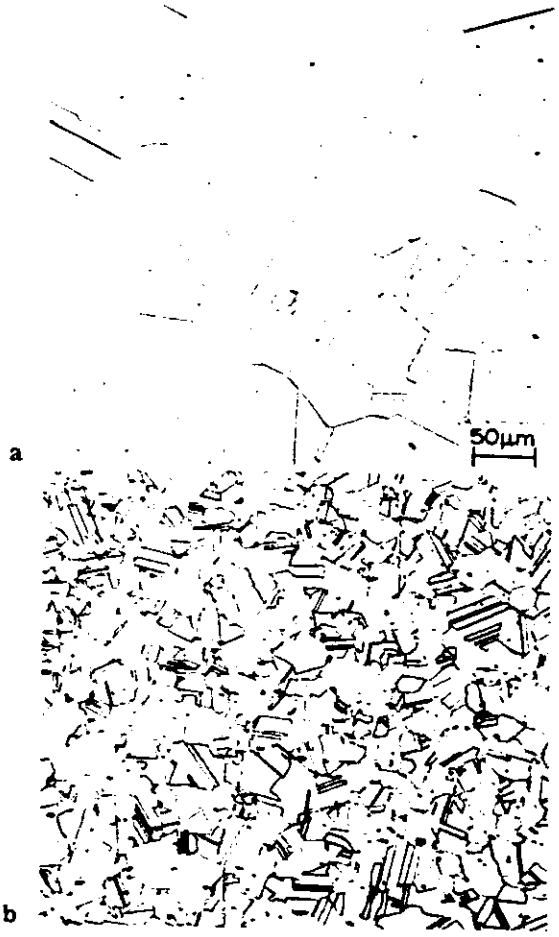

a high-purity vanadium; *b* ferrovanadium

26 Comparison of grain structures in LRO-37 prepared from different raw materials; heat treatment 20 min at 1150°C, 24 h at 650°C, 24 h at 600°C, 48 h at 550°C

Figure 32 shows the high-cycle fatigue behaviour of the titanium-modified alloys LRO-23 and LRO-37 as a function of temperature. Since the fatigue properties of LRO-23 at room temperature are not available, data for the base alloy LRO-1 are used in the plot. The fatigue resistance of LRO-1 and LRO-23 should not be very different, since both alloys exhibited transgranular fracture at room temperature. The fatigue life of the LRO alloys decreases with increasing stress amplitude $\Delta\sigma$ and test temperature. In comparison, the fatigue life of LRO-37 is much less dependent on test temperature. The fatigue resistance of the LRO alloys is superior to that of other ordered alloys. For example, at a fatigue life of 10^6 cycles, the LRO alloys can tolerate $\Delta\sigma$ values >50% higher than the ordered alloys FeCo and Ni_3Mn, at room temperature.[77]

At room temperature, all the fatigue specimens fractured transgranularly, with a very faceted appearance. Metallographic evidence indicated that microcracks were nucleated by slip bands and propagated along both slip bands and twin bands. At 600–650°C, the base alloy LRO-1 showed a mixed fracture mode, both intergranular and transgranular facets being visible (Fig. 33*a*), but the

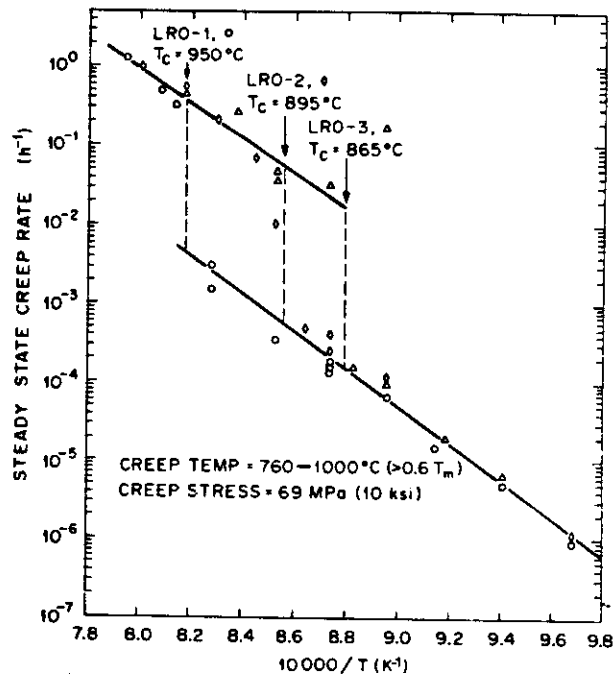

27 Variation of steady-state creep rate with temperature for Co-base LRO alloys

titanium-modified alloys exhibited predominantly transgranular fracture (Fig. 33*b*). Additions of titanium reduced the tendency toward intergranular cracking, thus improving the fatigue resistance of the LRO alloys. Limited TEM studies indicated[76] that titanium additions reduced the density of grain-boundary precipitation, so reducing the number of sites available for the nucleation of grain-boundary cracks. An added benefit of titanium could be the scavenging of harmful impurities segregated at grain boundaries.

At 850°C, the fracture path was essentially intergranular for both the base alloy LRO-1 and the titanium-modified LRO-23 (Fig. 33*c* and *d*). Nevertheless, the grain-boundary facets observed in LRO-23 were much rougher, dimples being visible in some areas.

Since resistance to fatigue is important for structural applications, it is worth while to compare the fatigue properties of LRO alloys with those of commercial alloys.[76] The temperature dependence of the maximum stress for a fatigue life of 10^6 cycles for LRO alloys is compared with those for the superalloys Inconel 617 and Incoloy 901 in Fig. 34. The fatigue resistance of the LRO alloys is superior to those of the commercial alloys below 700°C, and comparable at higher temperatures. The superiority of the LRO alloys at lower temperatures may be related to the increased difficulty of fatigue-crack nucleation in these alloys, caused by the restricted cross-slip in LRO lattices.[1] The ease of nucleation of grain-boundary cracks increases with increasing temperature, thereby lowering the fatigue resistance of the LRO alloys at higher temperatures. Further improvements in the fatigue resistance of LRO alloys will require means of suppressing the nucleation and propagation of fatigue cracks along the grain boundaries.

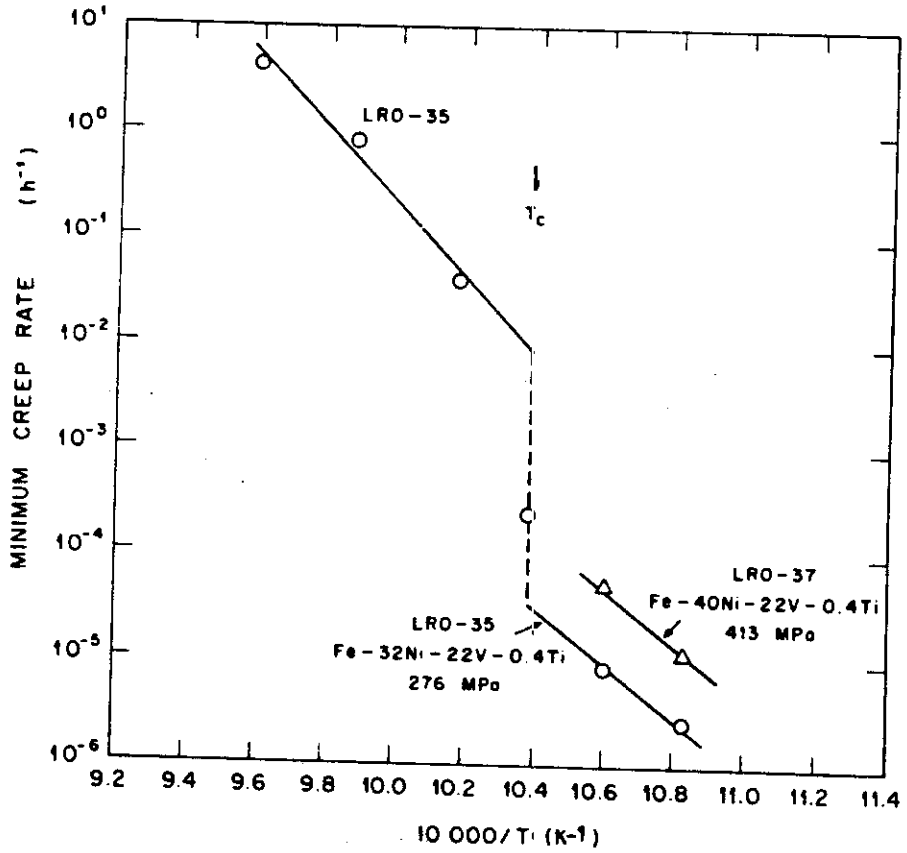

28 Variation of minimum creep rate with temperature and applied stress for Fe-base LRO alloys; after Liu[20]

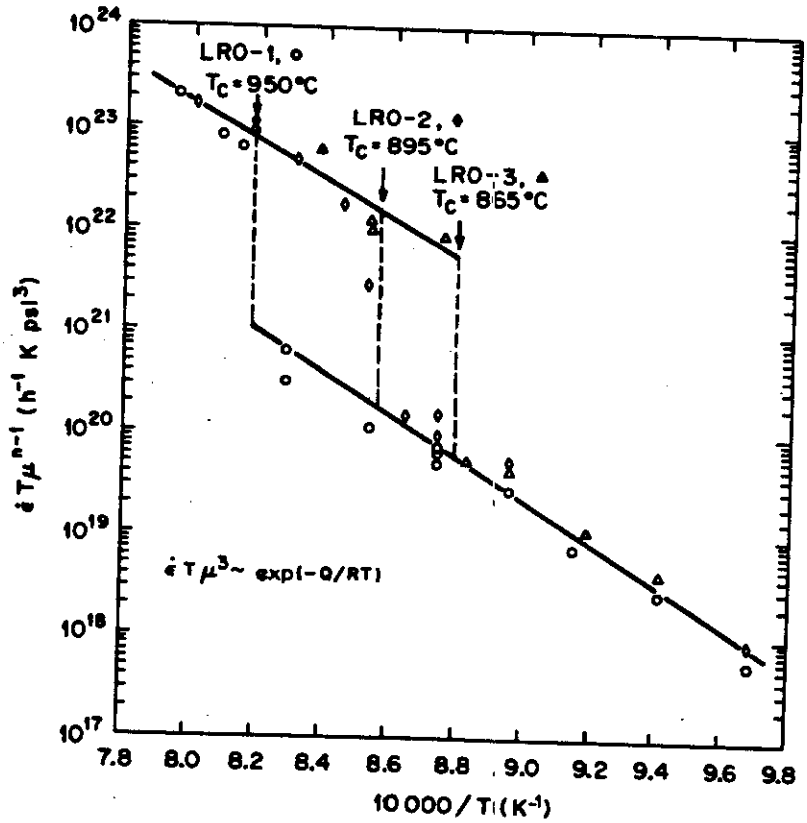

29 Variation of 'normalized' creep rate with temperature for LRO-1, LRO-2, and LRO-3 alloys at applied stress of 69 MNm^{-2} in temperature range 760–1000°C

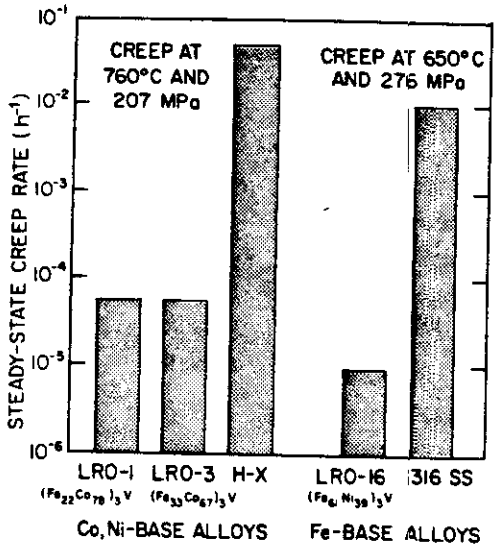

30 Comparison of steady-state creep rates of LRO alloys with those of commercial solid-solution strengthened alloys Hastelloy-X (H-X) and type 316 stainless steel

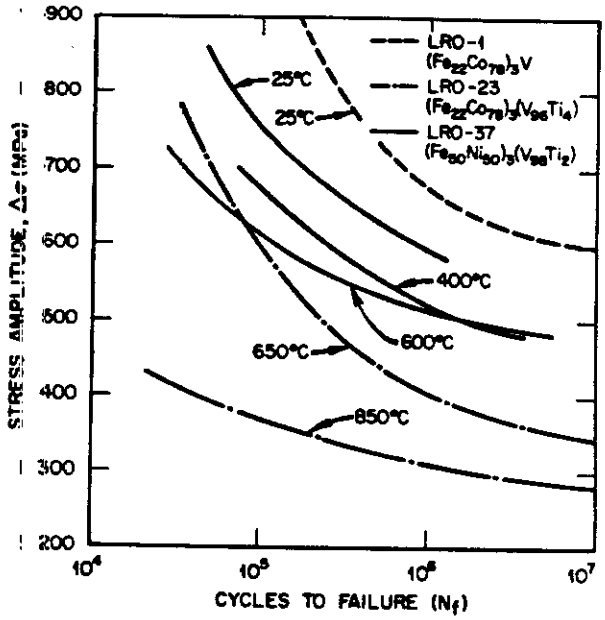

32 High-cycle fatigue data for base alloy LRO-1 and Ti-modified alloys LRO-37 and LRO-23; from Ashok *et al.*[76]

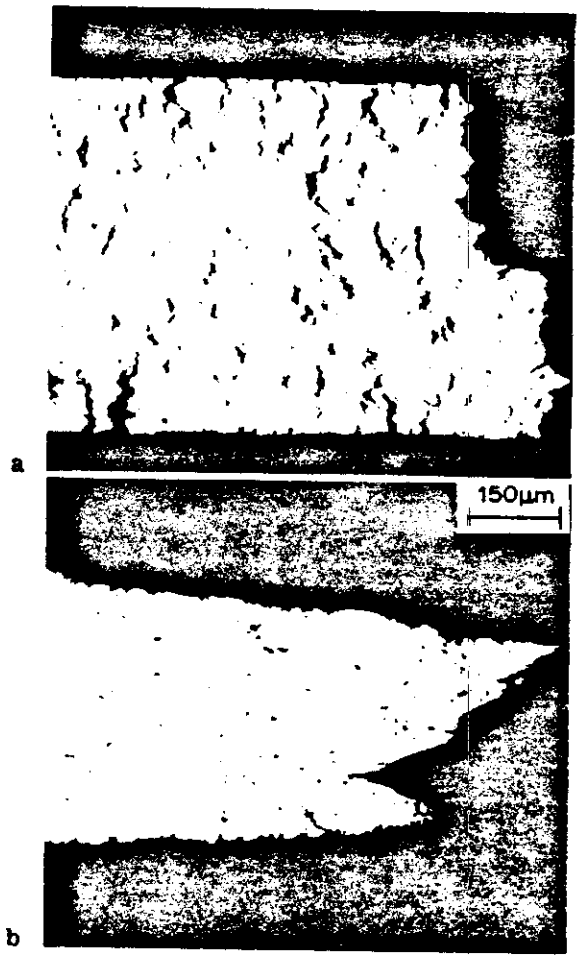

a brittle fracture of base alloy LRO-1; *b* ductile fracture of Ti-modified alloy LRO-34

31 Fracture behaviour of LRO alloys creep tested at 871°C with applied stress of 69 MNm^{-2}

4. ENVIRONMENT-RELATED PROPERTIES

4.1 Irradiation behaviour

The irradiation behaviour of LRO alloys has been studied by ion bombardment[78,79] and neutron irradiation.[78,80] The ion bombardment was performed on disc specimens irradiated to 70 dpa (displacements per atom) with 4 MeV nickel ions, while simultaneously being injected with 8 at.-ppmHe/dpa and 28 at.-ppmD/dpa at temperatures up to 750°C. Figure 35 is a plot of irradiation-induced swelling as a function of irradiation temperature, based on data from Braski.[78,81] Here, the LRO alloys containing no residual σ-phase showed little swelling in their ordered states. The interesting feature of this plot is that LRO-37 and LRO-20 swell sharply above 670°C, in accordance with their loss of LRO above that temperature. On the other hand, the alloy LRO-1 ($T_c \approx 950$°C) remained ordered and showed very low swelling at all temperatures up to 750°C. These results demonstrate that the LRO alloys are more resistant to swelling in the ordered than in the disordered state. Schulson[82] has pointed out that vacancies migrate with difficulty in ordered lattices, so interstitial–vacancy recombination processes during irradiation are more likely.

The swelling rate of type 316 stainless steel, irradiated under the same conditions as the LRO alloys, is also shown in Fig. 35 for comparison. It can readily be seen that the LRO alloys in the ordered state are more resistant to swelling than type 316 stainless steel. It should be noted that the type 316 stainless steel used by Braski had been cold worked to 20% reduction. Without this optimum amount of cold work, the swelling rate of type 316 stainless steel is substantially higher. Because of their good resistance to irradiation-induced swelling, LRO alloys appear to have poten-

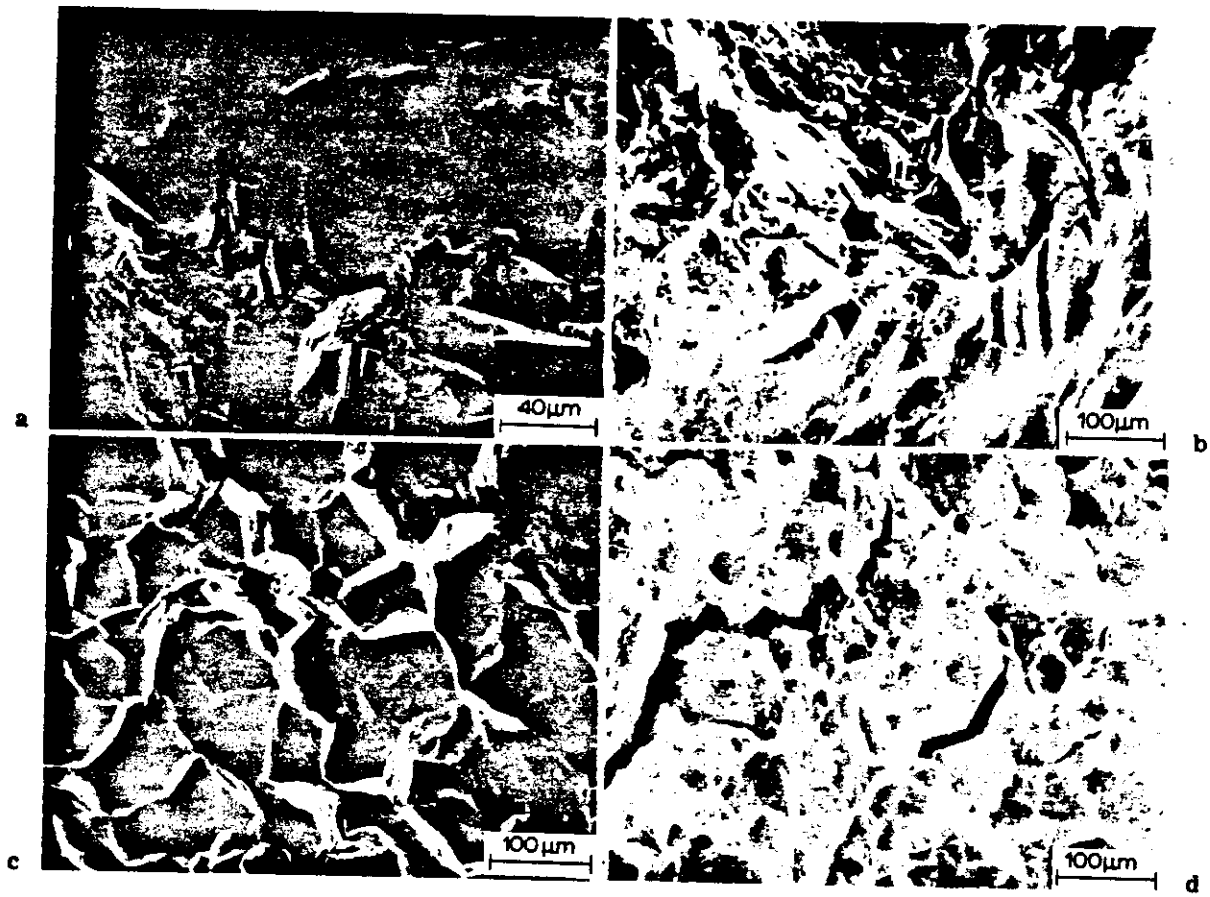

a LRO-1 fractured at 650°C; *b* LRO-23 fractured at 650°C; *c* LRO-1 fractured at 850°C; *d* LRO-23 fractured at 850°C

33 Fatigue fractographs of various LRO alloys; from Ashok *et al.*[76]

tial for use as structural materials for nuclear applications.

Microstructural examination revealed that ion bombardment altered the domain size and the precipitation of VC, and induced other microstructural changes. A high density of dislocations and faulted loops was observed; the size of the loops increased with irradiation temperature. The loops were mainly interstitial, and were probably formed through condensation of interstitials. Many of the VC particles in the matrix were dissolved, while the VC particles on grain boundaries were coarsened during ion bombardment. Irradiation

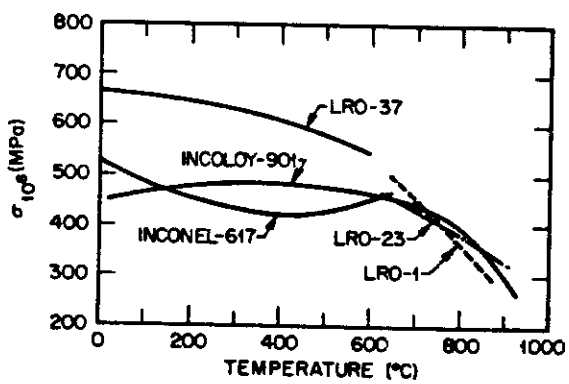

34 Variation of maximum stress for fatigue life of 10^6 cycles σ_{10^6} with temperature for LRO alloys and commercial superalloys; from Ashok *et al.*[76]

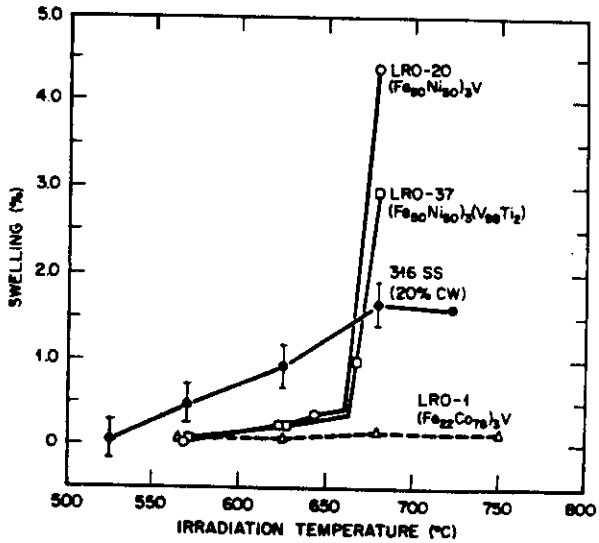

35 Variation of irradiation-induced swelling with irradiation temperature for LRO alloys and type 316 stainless steel (cold worked to 20% reduction) following 4 MeV nickel-ion irradiation to 70 dpa with simultaneous injection of helium and deuterium; after Braski[78,81]

a superlattice dark-field micrograph of unirradiated specimen using (100) reflection, showing domains and antiphase boundary; *b* dark-field micrograph of specimen ion-bombarded to 70 dpa at 570°C, showing domains

36 Comparison of domain structures observed in unirradiated and ion-bombarded LRO-1 specimens; from Braski and Farrell[79]

at lower temperatures markedly reduced the ordered-domain size, as is shown in Fig. 36. Many of the new domain boundaries were composed of the newly created faulted loops.[78,79] It is also possible that irradiation lowers the LRO parameter and provides additional disordered regions for domain walls.

Tensile properties of LRO-16 were determined after neutron irradiation[78,80] in the Oak Ridge Reactor at 250, 350, and 550°C, to a damage level of 3.8 dpa and a helium level of 29 at.-ppm. Unfortunately, LRO-16 samples contained a small amount of residual σ-phase introduced during cooling through the wide $\gamma + \sigma$ phase field. The presence of σ-phase is undesirable in LRO alloys because it embrittles the grain boundaries. Also, the formation of σ-phase draws vanadium atoms from solution, thus weakening the atomic ordering in the matrix. The neutron irradiation increased σ_y and lowered the ductility of the LRO alloys, but produced relatively little swelling (~0.07% at 550°C). The hardening was apparently produced by the formation of small interstitial loops and numerous dislocations. The loss of ductility was accompanied by a change in fracture mode from transgranular to intergranular. Possible explanations for the weakened grain boundaries include the presence of helium and σ-phase particles at the grain boundaries, helium embrittlement, and increased segregation of impurities (such as sulphur) to the boundaries. Braski[81] has studied the post-irradiation mechanical properties of σ-free titanium-modified alloy LRO-37.

4.2 Hydrogen embrittlement

The influence of a hydrogen environment on the mechanical properties of ordered alloys has not been well documented. In view of this, hydrogen embrittlement in LRO alloys was studied by hydrogen exposure in a high-pressure autoclave[67] and by cathodic charging[83] of hydrogen in 1N H_2SO_4 at a current density of 500 Am^{-2}. Table 4 gives the effect of hydrogen charging on the tensile properties of fully ordered LRO-37 and LRO-35 samples exposed to high-pressure (9.7–10.3 MPa) H_2 at 517 or 548°C in the autoclave. The hydrogen exposure moderately reduced the elongation at room temperature, but did not affect the ductility at and above 200°C. The room-temperature ductility was fully restored after a vacuum heat

Table 4 Room-temperature tensile ductility of LRO alloys exposed to high-pressure hydrogen

Alloy	Treatment time, h	Treatment temp., °C	H_2 pressure, MPa	Test temperature	Tensile elongation, %
LRO-37	0	...	0	Ambient	41.8
	1440	548	10.3	Ambient	19.4
	1	600	Vacuum	Ambient	43.8
LRO-35	0	...	0	Ambient	42.1
	148	577	9.7	Ambient	15.1
	0	...	0	200°C	35.0
	148	517	9.7	200°C	33.0
	0	...	0	650°C	33.6
	148	517	9.7	650°C	35.5

Table 5 Tensile properties of ordered and disordered LRO-42 specimens tested in air and hydrogen at ambient temperature; after Kuruvilla *et al.*[83]

Environment	Strength, MNm^{-2} Yield	Ultimate	Elongation, %
Ordered Alloy			
Air	344	1175	25
Hydrogen	344	485	13
Disordered Alloy			
Air	415	770	38
Hydrogen	415	710	30

treatment of 1 h at 600°C. This restoration of the ductility strongly suggests that the hydrogen embrittlement is not caused by damage to the microstructure (e.g. formation of methane bubbles), but is instead caused by retention of a small amount of hydrogen, which can be readily 'pumped out' by vacuum treatment.

Kuruvilla *et al.*[83] have recently determined the effect of LRO on hydrogen embrittlement in LRO-42 alloy, which has the same composition as LRO-37, except for trace additions of rare earth metals. The LRO-42 specimens, in both ordered and disordered conditions, were charged with hydrogen and then tested in tensile, delayed-failure, and cyclic-loading tests in air and in hydrogen. The results indicated that hydrogen embrittlement was more severe in the ordered material for each of the three types of test. As for the room-temperature tensile data, given in Table 5, hydrogen charging caused a reduction in ductility of nearly 50% for the ordered samples, but the reduction was only 20% for the disordered samples. Fractographic examination by scanning electron microscopy revealed a strong tendency toward intergranular fracture in the ordered material in the presence of hydrogen, but the fractographic features changed much less in the disordered samples (Fig. 37). Planar slip (leading to increased dislocation transport of hydrogen), coupled with greater impurity segregation at grain boundaries, have been suggested as possible mechanisms to explain the greater severity of hydrogen embrittlement in the ordered condition.

Berkowitz and Miller[84] have recently characterized hydrogen embrittlement in Ni_2Cr as a function of the LRO parameter S. Their tests indicated that Ni_2Cr was highly susceptible to hydrogen embrittlement in both the fully disordered and ordered conditions. The diminution in reduction of area in both conditions was about 70%. However, the alloy showed a minimum susceptibility to hydrogen embrittlement for a partially ordered state with $S = 0.4$–0.5. The alloy undergoes a phase transition upon ordering, which complicates the analysis of hydrogen embrittlement. The present LRO alloys are considered to be more suitable for studying the effect of LRO on hydrogen embrittlement because their order → disorder transformations do not involve a change in lattice structure.

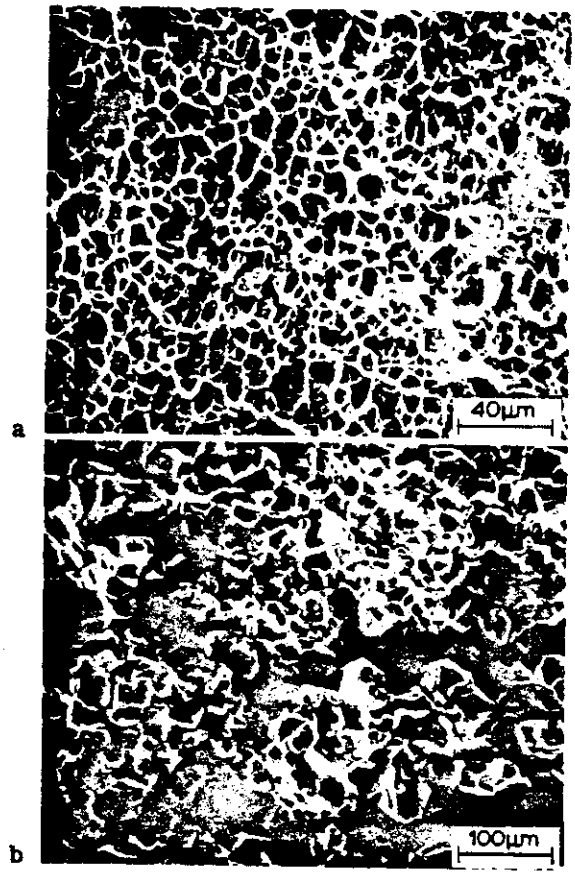

a disordered state; *b* ordered state

37 Scanning electron fractographs of LRO-42 samples tested in tension in hydrogen environments; from Kuruvilla *et al.*[83]

4.3 Oxidation and corrosion behaviour

Limited experiments have been conducted to study the oxidation and corrosion behaviour of LRO alloys in air,[16] superheated-steam,[85] liquid-lithium,[86] and oxidizing–sulphidizing[87] environments. Figure 38 shows log–log plots of weight gain against exposure time for LRO alloys oxidized isothermally at 500–760°C. The alloys exhibited parabolic oxidation, the slopes of the curves being ~0.5. The oxidation rate appears to be quite independent of alloy composition, as is indicated by the similar weight gains for LRO-1 and LRO-2 in Fig. 38.

Spalling was observed on the LRO alloys during cooling, following extensive air oxidation above 600°C. The spalling is believed to have resulted from a large mismatch between the coefficients of thermal expansion and poor bonding between the oxide scale and base metal. Electron-microprobe examination of the oxide scale formed on LRO-1 revealed three distinct layers, according to the distributions of Co, Fe, and V (Fig. 39). The outermost layer (A) was depleted in iron and vanadium, and X-ray-diffraction data indicated that this layer consisted of almost 100% cobalt oxides. At least two types of cobalt oxide existed in this layer, which showed different contrast. The middle layer (B) was enriched with iron, and the inner layer (C) with vanadium. Line scanning

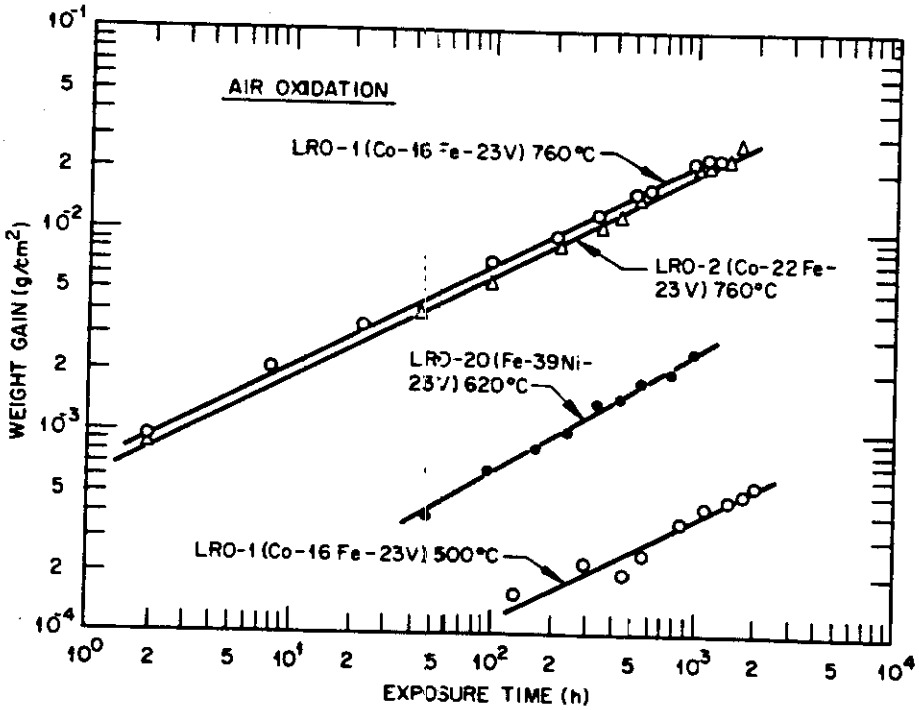

38 Variation of weight gain with exposure time for LRO alloys oxidized in air

indicated the existence of cobalt in all three layers. The macrocracks formed developed essentially in the inner layer. With regard to the standard free energy of formation,[88] the vanadium oxide is the most stable, whereas cobalt oxide is the least stable. The observed distributions of major elements suggest that cobalt atoms diffuse from the interior to the surface, where the oxygen potential is high enough to oxidize cobalt.

The LRO alloys showed excellent resistance to superheated-steam corrosion at 540°C (Ref. 85). This is indicated in Fig. 40, in which the weight changes of LRO-1 and LRO-17 are compared with those of type 304 stainless steel and 2.25Cr–1Mo ferritic steel. All the alloys showed weight gains caused by oxidation. The oxidation rates of the LRO alloys are even lower than that of type 304 stainless steel. This result is unexpected because

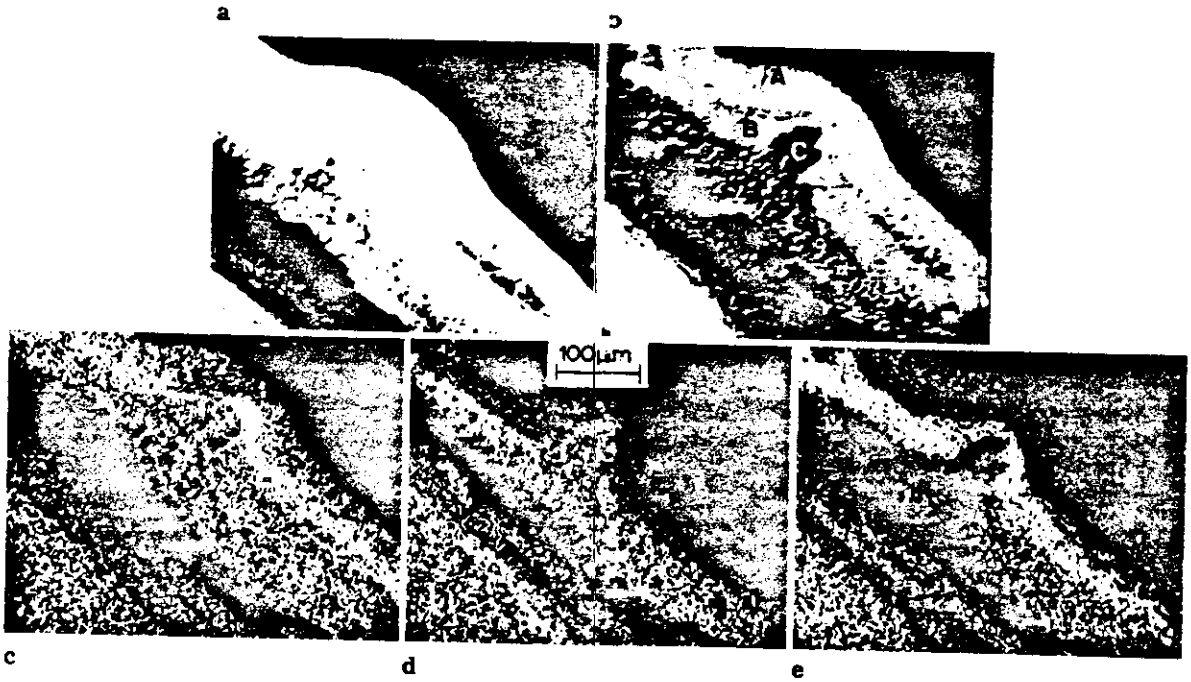

a optical micrograph; *b* back-scattered electron micrograph; *c* Co $K\alpha$ EDAX picture; *d* V $K\alpha$ EDAX picture; *e* Fe $K\alpha$ EDAX picture

39 Microstructure and distribution of elements in oxide layer, as determined by energy-dispersive X-ray analysis (EDAX), for LRO-1 oxidized in air at 760°C for 2400 h

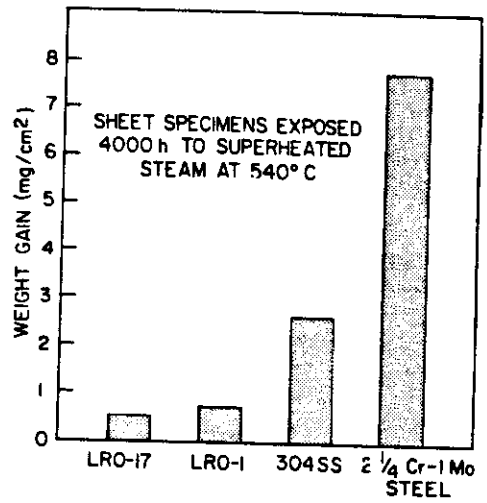

40 **Comparison of weight gains following exposure to superheated steam of LRO alloys with commercial type 316 stainless steel and 2.25Cr—1Mo ferritic steel; from Griess *et al.*[85]**

the LRO alloys contain no chromium, whereas type 304 stainless steel has 18–20%Cr in solution.

Corrosion of LRO alloys in liquid lithium[86] and sulphidizing[87] environments is currently being studied at Oak Ridge National Laboratory. The LRO alloys containing up to 40%Ni showed very low weight loss and no change in microstructure after exposure for several thousand hours at 500 and 600°C in static lithium encapsulated by the same alloys. The weight losses in LRO-35 and LRO-37 were actually lower than that of Incoloy 800 (containing 32%Ni) by two orders of magnitude. Tensile tests at temperatures up to 600°C also indicated that the mechanical properties of the LRO alloys were not affected by lithium exposure. However, the LRO alloys exhibited much higher weight losses when exposed to lithium loops made of stainless steel (depleted in nickel) or to static lithium in ferritic steel capsules. The high corrosion rates in these cases may be caused by mass transport (mainly of nickel) between dissimilar metals. Both LRO-1 and LRO-37 samples were exposed to hostile environments at sulphur pressures between 10^{-2} and 10^{-8} atm and oxygen pressures of 10^{-2} to 10^{-14} atm. To protect the alloys from excessive corrosion, a set of specimens was coated with iron—chromium—aluminium layers by a slurry technique at Lockheed Palo Alto Research Laboratory, Palo Alto, Calif. The preliminary results are very encouraging. The corrosion behaviour of the uncoated LRO specimens (containing no chromium) is comparable to that of Haynes 188 (containing 22%Cr) after 100 h exposure at 850°C. The coated specimens did not show any sulphidation attack.

The LRO alloys generally showed limited oxidation resistance at high temperatures in strongly oxidizing environments, such as air. This is because alloys containing no chromium or aluminium are incapable of forming a protective oxide scale that can serve as an effective barrier in impeding the inward diffusion of oxygen and outward diffusion of metallic elements. The oxidation rates of current LRO alloys are substantially higher than those of austenitic stainless steels, but lower than those of ferritic steels (such as 2.25Cr—1Mo steel). Work is in progress on improving the oxidation resistance of LRO alloys through alloy additions and surface coatings.[67]

5. POTENTIAL APPLICATIONS

LRO alloys based on $(Fe,Co,Ni)_3(V,Ti)$ constitute a new class of structural materials having a unique combination of high-temperature strength, ductility, workability, and long-term structural stability. Unlike conventional alloys, the yield strength of LRO alloys increases with temperature above 300°C, reaching a maximum around T_c (650–1000°C). Because of this increase, the LRO alloys are substantially stronger than commercial solid-solution strengthened alloys at elevated temperatures (Fig. 16). The use of LRO alloys should be limited to temperatures below T_c, since the alloys show a sharp drop in strength above this temperature, owing to the loss of LRO.

Since current LRO alloys have limited oxidation resistance in air above 600°C, they would best be used as structural materials in reducing (e.g. H_2), neutral (e.g. vacuum), inert (e.g. He, Ar), or slightly oxidizing (e.g. steam) environments. Potential applications include their use as improved hot-section components in conventional power plants and advanced closed-cycle energy-conversion systems such as (1) advanced heat engines — Stirling engines (using H_2 or He as the working medium) and other high-temperature systems, (2) advanced steam power plants — steam generators and turbines, (3) nuclear process heat systems — ducting and heat exchangers, and (4) closed-cycle solar-power systems. The LRO alloys $(Fe,Ni)_3(V,Ti)$ possess excellent high-temperature strength, creep properties, and fatigue resistance, in combination with superior corrosion resistance in steam environments. In view of this, these alloys are particularly suitable for steam-turbine applications.

The LRO alloys are also resistant to irradiation-induced swelling, as shown in Fig. 35. A combination of excellent high-temperature properties with resistance to irradiation damage makes LRO alloys promising as materials for nuclear-industry applications.

6. SUMMARY

This paper has provided a comprehensive review of the physical metallurgy and mechanical properties of long-range-ordered (LRO) alloys based on the quasiternary system Fe_3V–Co_3V–Ni_3V. Ordered crystal structures in $(Fe,Co,Ni)_3V$ alloys are built up by stacking close-packed, ordered layers, but differ in their stacking sequences. The stacking character of the ordered structures can be altered systematically by controlling the alloy electron density (e/a), defined as the number of valence electrons per atom. As e/a decreases, the stacking character changes

from purely hexagonal, through different, ordered mixtures of hexagonal and cubic layers, to purely cubic. Partial replacement of cobalt and nickel atoms with iron atoms lowers e/a in the alloys and stabilizes the ordered structure with a cubic stacking character. With suitable control of e/a, the $L1_2$-type cubic ordered structure is stabilized in the $(Fe,Co)_3V$, $(Fe,Co,Ni)_3V$, and $(Fe,Ni)_3V$ alloy systems.

The LRO alloys with the cubic ordered structure can be fabricated and welded by conventional processing techniques. Two types of phase relationship were observed in the LRO alloys, depending on alloy composition (Fig. 7). For the type-I phase relationship, the disordered solid solution γ transforms to the cubic ordered γ' below the critical ordering temperature T_c. For the type-II phase relationship, the γ solid solution starts to precipitate σ-phase at temperatures below the peak temperature for σ-phase precipitation T_1, and the two phases transform to the ordered γ' through the peritectoid reaction $\gamma + \sigma \rightarrow \gamma'$ below T_c. The T_c values of the LRO alloys vary from 650 to 1000°C, decreasing with increasing iron content. The σ-phase field can be completely suppressed as a stable entity in LRO alloys if e/a exceeds 7.79 in $(Fe,Co)_3V$ or 8.01 in $(Fe,Ni)_3V$ alloys (Fig. 9).

Small VC-type carbide particles were observed within grains and along grain boundaries in both disordered and ordered specimens. Domain structures and stacking faults were observed only in ordered specimens aged below T_c. Evidence from transmission electron microscopy indicated that both intrinsic and extrinsic stacking faults were nucleated at VC particles by the punching out of perfect dislocations, which subsequently dissociated into Shockley partials (for intrinsic faults) or Frank and Shockley partials (for extrinsic faults). The domain boundaries appear wavy, indicating that the antiphase-boundary energy is quite isotropic.

The room-temperature tensile ductility of $(Fe,Co,Ni)_3V$ alloys was strongly influenced by the ordered crystal structure. The alloys with multilayered hexagonal ordered structures exhibited brittle fracture with little ductility, while those with the cubic ordered structure were ductile with tensile elongations exceeding 35% at room temperature. The ductility of the cubic ordered alloys is independent of alloy composition until the cobalt content exceeds 60 at.-%.

The yield behaviour of LRO alloys was characterized as a function of test and quench temperatures. Unlike conventional alloys, the yield strength of LRO alloys increases with temperature and peaks around T_c. The room-temperature yield strength, on the other hand, is not sensitive to quench temperature, except in the vicinity of T_c. Calculation of the yield-stress increase as a function of test temperature strongly suggests that the anomalous temperature dependence of yielding in LRO alloys is caused by a thermally activated process, rather than a disordering effect.

The base LRO alloys $(Fe,Co,Ni)_3V$ showed a decrease in ductility above 400–700°C (depending on alloy composition), and their ductility reached a minimum near T_c. Corresponding to the decrease, the fracture mode exhibited a transition from transgranular to intergranular. Modifying the base alloys with titanium significantly improved the ductility at elevated temperatures. Titanium additions also improved the creep-rupture ductility of LRO alloys.

The creep behaviour of LRO alloys can be described by the rate equation given as equation (2) above. All the alloys exhibited a discontinuous change in creep rate $\dot{\epsilon}$ in the vicinity of T_c. Extrapolation of data from above T_c to below T_c reveals that the formation of LRO lowers $\dot{\epsilon}$ by two orders of magnitude. This decrease in $\dot{\epsilon}$ makes the LRO alloys extremely creep resistant in the ordered condition. The values of n and Q in equation (2) for ordered LRO-1, LRO-2, and LRO-3 were measured to be 4 and 393 kJmol^{-1}, respectively.

The high-cycle fatigue properties of base LRO alloys are quite sensitive to test temperature, and show considerable heat-to-heat variation. This behaviour results from the tendency toward grain-boundary fracture, which can be alleviated, to a certain extent, by adding small amounts of titanium. The fatigue resistance of the LRO alloys is superior to those of commercial superalloys, such as Inconel 617 and Incoloy 901, below 700°C, and comparable at higher temperatures.

The LRO alloys showed low swelling in their ordered state under dual-beam ion bombardments. The alloys displayed a sharp increase in irradiation-induced swelling above T_c, corresponding to the loss of LRO. The ion bombardment also reduced domain size, altered precipitation of VC, and induced other microstructural changes such as the appearance of high densities of dislocations and fault loops. Neutron irradiation increased the yield strength and lowered the ductility of LRO-16, but produced relatively little swelling. The hardening was apparently produced by the formation of small interstitial loops and numerous dislocations. The loss of ductility was accompanied by a change from transgranular to intergranular fracture.

Exposure to high-pressure hydrogen at 517–548°C caused a moderate reduction in tensile elongation of $(Fe,Ni)_3V$ alloys at room temperature, but did not affect their ductility at or above 200°C. Following exposure to hydrogen environments produced by cathodic charging, LRO-37 exhibited more severe embrittlement in the ordered than in the disordered condition. Examination by scanning electron microscopy revealed a strong tendency toward intergranular fracture in the ordered samples in the presence of hydrogen, but fractographic features changed much less in the disordered samples.

Limited experiments were conducted to study the oxidation and corrosion behaviour of LRO alloys in various environments. Current LRO alloys had a limited oxidation resistance in air above 600°C, but showed an excellent resistance to superheated-steam corrosion at 540°C. The LRO alloys, with their combination of high-temperature strength, ductility, workability, and creep and fatigue resistance, have great potential as structural materials in inert and slightly oxidizing (e.g. steam) environments.

ACKNOWLEDGMENTS

The author wishes to express his sincere thanks to Dr D.N. Braski, Dr C.C. Koch, and Dr N.S. Stoloff for providing the original micrographs used in this review. Thanks are also due to Dr D.N. Braski, Dr A. DasGupta, Dr C.C. Koch, Dr J.O. Stiegler, and Dr A.C. Schaffhauser for reviewing the manuscript. The author is also grateful to S. Peterson and Connie Dowker, respectively, for their work in editing and preparing the manuscript.

REFERENCES

1. N.S. Stoloff and R.G. Davies: *Prog. Mater. Sci.*, 1966, **13**, (1), 1–84.
2. B.H. Kear, C.T. Sims, N.S. Stoloff, and J.H. Westbrook, (eds.): 'Ordered alloys'; 1970, Baton Rouge, La, Claitor's Publishing Division.
3. H. Warlimont, (ed.): 'Order–disorder transformation in alloys'; 1974, New York, Springer-Verlag.
4. J.H. Westbrook: *Metall. Trans.*, 1977, **8A**, 1327–1360.
5. P.H. Thornton, R.G. Davies, and T.L. Johnston: *Metall. Trans.*, 1970, **1**, 207.
6. S.M. Copley and B.H. Kear: *Trans. AIME*, 1967, **239**, 977.
7. N.S. Stoloff and R.G. Davies: *Acta Metall.*, 1964, **12**, 473.
8. S.J. Liang and D.P. Pope: *Acta Metall.*, 1977, **25**, 485–493.
9. C. Lall, S. Chin, and D.P. Pope: *Metall. Trans.*, 1979, **10A**, 1323.
10. L.E. Tanner *et al.*: 'Mechanical behaviour of intermetallic compounds', Report AST–TDR62–1087, Parts I–III, Man Labs Inc., Cambridge, Mass., 1963–1964.
11. E.M. Schulson and M.J. Stewart: *Metall. Trans.*, 1976, **7B**, 363.
12. E.M. Schulson: *J. Nucl. Mater.*, 1975, **56**, 38.
13. K. Aoki and O. Izumi: *Acta Metall.*, 1979, **27**, 807.
14. H.A. Lipsett, D. Shechtman, and R.E. Shafrik: *Metall. Trans.*, 1980, **11A**, 1369.
15. T.L. Johnston, R.G. Davies, and N.S. Stoloff: *Philos. Mag.*, 1965, **12**, 305.
16. A.U. Seybolt and J.H. Westbrook: *Acta Metall.*, 1964, **12**, 449.
17. J.H. Westbrook and D.L. Wood: *J. Inst. Met.*, 1962–1963, **91**, 174–182.
18. C.T. Liu and H. Inouye: *Metall. Trans.*, 1979, **10A**, 1515.
19. C.T. Liu: *J. Nucl. Mater.*, 1979, **85/86**, 907.
20. C.T. Liu: *J. Nucl. Mater.*, 1982, **104**, (1–3, Part B), 1205.
21. C.T. Liu: *Metall. Trans.*, 1973, **4**, 1743.
22. P.A. Beck: *Adv. X-ray Anal.*, 1969, **12**, 1.
23. A.K. Sinha: *Trans. AIME*, 1969, **245**, 911.
24. B.C. Giessen and N.J. Grant: *Acta Crystallogr.*, 1965, **18**, 1080.
25. H. Sato, R.S. Toth, and G. Honjo: *J. Phys. Chem. Solids*, 1969, **28**, 137.
26. J.H. Van Vucht and K.H. Buschow: *J. Less-Common Met.*, 1965, **10**, 98.
27. J.H.N. Van Vucht: *J. Less-Common Met.*, 1966, **11**, 308.
28. E.E. Havinga, J.H.N. Van Vucht, and K.H.J. Buschow: in Ref. 2, pp. 111–124.
29. R.M. Waterstrat: *Metall. Trans.*, 1973, **4**, 455.
30. P.J. Meschter and W.L. Worrell: *Metall. Trans.*, 1976, **7A**, 299.
31. A.E. Dwight and P.A. Beck: *Trans. AIME*, 1959, **215**, 976.
32. A.K. Sinha: *Prog. Mater. Sci.*, 1972, **15**, (2), 81–185.
33. S. Saito: *Acta Crystallogr.*, 1959, **12**, 500.
34. S.A. David, D.N. Braski, and C.T. Liu: Oak Ridge National Laboratory, unpublished results, 1982.
35. H.P. Stuwe: *Trans. AIME*, 1959, **215**, 408.
36. R.E. Hanneman and A.N. Mariano: *Trans. AIME*, 1964, **230**, 937.
37. H.J. Murphy, C.T. Sims, and A.M. Beltran: *J. Met.*, 1968, **20**, 46.
38. L.R. Woodyatt, C.T. Sims, and J.H. Beattie: *Trans. AIME*, 1966, **236**, 519.
39. D.N. Braski, R.W. Carpenter, and J. Bentley: *Acta Metall.*, 1982, **30**, 799.
40. F. Touray, Y. Calvayrac, and M. Fayard: *C.R. Hebd. Séances Acad. Sci.*, 1971, **272**, 1196.
41. J.M. Silcock and N.J. Tunstall: *Philos. Mag.*, 1964, **10**, 360.
42. D.J.H. Cockayne, I.L.F. Ray, and M.J. Whelan: *Philos. Mag.*, 1969, **20**, 1265.
43. M.J. Marcinkowski and D.S. Miller: *Philos. Mag.*, 1961, **6**, 871.
44. R.G. Davies and N.S. Stoloff: *Acta Metall.*, 1963, **11**, 1347.
45. Y. Calvayrac and M. Fayard: *Phys. Status Solidi (a)*, 1973, **17**, 407.
46. G.J.L. Van der Wegen, P.M. Bronsvelt, and J.Th.M. de Hosson: *Metall. Trans.*, 1981, **12A**, 2125.
47. B.H. Kear: *Acta Metall.*, 1964, **12**, 555.
48. C.T. Liu and E.H. Lee: Proc. Metallurgical Society of AIME Annual Meeting, Chicago, Ill., Feb. 1981.
49. E.H. Lee, C.C. Koch, and C.T. Liu: in 'Rapidly solidified amorphous and crystalline alloys', 375–379; 1982, New York, Elsevier North-Holland.
50. M.J. Marcinkowski: in Ref. 3, pp. 364–403.
51. R.W. Cahn and J.A. Coll: *Acta Metall.*, 1961 **9**, 138.
52. C.T. Liu: Proc. Metallurgical Society of AIME Annual Meeting, Las Vegas, Nev., Feb. 1980.
53. G.W. Ardley: *Acta Metall.*, 1955, **3**, 525.
54. D.P. Pope: *Philos. Mag.*, 1972, **25**, 917.
55. E. Kunamoto and D.P. Pope: *Philos. Mag.*, 1976, **33**, 625.
56. R.A. Mulford and D.P. Pope: *Acta Metall.*, 1973, **21**, 1375.
57. P.A. Flinn: *Trans. AIME*, 1960, **218**, 145.
58. R.G. Davies and N.S. Stoloff: *Trans. AIME*, 1965, **233**, 714.
59. S. Takeuchi and E. Kuramoto: *Acta Metall.*, 1973, **21**, 415.
60. S. Takeuchi and E. Kuramoto: *J. Phys. Soc. Jpn*, 1971, **31**, 1282.
61. E. Kuramoto and D.P. Pope: *Acta Metall.*, 1978, **26**, 207.
62. B.H. Kear and H.G.W. Wilsdorf: *Trans. AIME*, 1962, **224**, 382.

63. J.W.Cable and C.T.Liu: Oak Ridge National Laboratory, unpublished results, 1982.
64. D.P.Pope: personal communication, University of Pennsylvania, Philadelphia, Pa, 1982.
65. C.T.Liu and E.M.Schulson: *Metall. Trans.*, 1984, **15A**, 701.
66. E.M.Schulson: *Metall. Trans.*, 1978, **9A**, 527.
67. C.T.Liu: Oak Ridge National Laboratory, unpublished results, 1982.
68. W.C.Johnson, J.E.Doherty, B.H.Kear, and A.F.Giamei: *Scr. Metall.*, 1974, **8**, 971.
69. T.Suzuki and M.Yamamoto: *J. Phys. Soc. Jpn*, 1959, **14**, 463.
70. J.Weertman: *ASM Trans. Q.*, 1968, **61**, 681.
71. M.Herman and N.Brown: *Trans. AIME*, 1965, **206**, 604.
72. J.A.Hren: PhD thesis, Stanford University, 1962, as cited in Ref. 1.
73. J.A.Hren and O.D.Sherby: *Appl. Mater. Res.*, 1965, **4**, 41.
74. C.R.Brinkman *et al.*: 'Application of Hastelloy X in gas-cooled reactor systems', Report ORNL/TM–5405, Oak Ridge National Laboratory, Oak Ridge, Tenn., 1976.
75. V.K.Sikka *et al.*: 'Use of ultimate tensile strength to correlate and estimate creep and creep-rupture behaviour of type 304 and 314 stainless steel', Report ORNL–5285, Oak Ridge National Laboratory, Oak Ridge, Tenn., Oct. 1977.
76. S.Ashok, K.Kain, J.M.Tartaglia, and N.S. Stoloff: *Metall. Trans.*, 1983, **14A**, 1997.
77. R.C.Broettner, N.S.Stoloff, and R.G.Davies: *Trans. AIME*, 1966, **236**, 131.
78. D.N.Braski: *J. Nucl. Mater.*, 1982, **104**, 1199.
79. D.N.Braski and K.Farrell: Proc. 'Electron microscopy 1980', 7th European Cong., Leiden, 1980, Vol. 1, 284.
80. D.N.Braski: in 'Effects of radiation on materials', (ed. H.R.Brager and J.S.Perrin), STP 782, 325; 1982, Philadelphia, Pa, American Society for Testing and Materials.
81. D.N.Braski: Oak Ridge National Laboratory, unpublished results, 1983.
82. E.M.Schulson: *J. Nucl. Mater.*, 1977, **66**, 322.
83. A.K.Kuruvilla, S.Ashok, and N.S.Stoloff: Proc. 3rd Int. Cong. on 'Hydrogen and materials', Paris, June 1982, Ecole Centrale des Arts et Manufactures.
84. B.J.Berkowitz and C.Miller: *Metall. Trans.*, 1980, **11A**, 1877.
85. J.C.Griess, C.T.Liu, and J.H.DeVan: Oak Ridge National Laboratory, unpublished results, 1982.
86. P.F.Tortorelli, J.H.DeVan, and C.T.Liu: 'Corrosion of austenitic, ferritic, and long-range ordered alloys in flowing lithium', ADIP Semiannual Progress Report DOE/ER–0045/8, US Department of Energy, Washington, DC, 1982.
87. P.J.Ficalora and J.H.DeVan: Oak Ridge National Laboratory, unpublished results, 1982.
88. O.Kubaschewski and C.B.Alcock: 'Metallurgical thermochemistry', 5 edn; 1979, New York, Pergamon.

© 1984 The Metals Society and the American Society for Metals